Polyhedron 180 (2020) 114379

Contents lists available at ScienceDirect

Polyhedron

journal homepage: www.elsevier.com/locate/poly

Enhancing easy-plane anisotropy in bespoke Ni(II) quantum magnets

Jamie L. Manson [a,*], Zachary E. Manson [a], Ashley Sargent [a], Danielle Y. Villa [a], Nicole L. Etten [a], William J.A. Blackmore [b], Samuel P.M. Curley [b], Robert C. Williams [b], Jamie Brambleby [b], Paul A. Goddard [b,*], Andrew Ozarowski [c], Murray N. Wilson [d], Benjamin M. Huddart [d], Tom Lancaster [d], Roger D. Johnson [e], Stephen J. Blundell [e], Jesper Bendix [f], Kraig A. Wheeler [g], Saul H. Lapidus [h], Fan Xiao [i,j], Serena Birnbaum [k], John Singleton [k,*]

[a] Department of Chemistry, Biochemistry & Physics, Eastern Washington University, Cheney, WA 99004, USA
[b] Department of Physics, University of Warwick, Coventry CV4 7AL, UK
[c] National High Magnetic Field Laboratory, Florida State University, Tallahassee, FL 32310, USA
[d] Center for Materials Physics, Department of Physics, Durham University, Durham DH1 3LE, UK
[e] Clarendon Laboratory, Department of Physics, University of Oxford, Oxford OX1 3PU, UK
[f] Department of Chemistry, University of Copenhagen, DK 2100 Copenhagen, Denmark
[g] Department of Chemistry and Biochemistry, Whitworth University, Spokane, WA 99251, USA
[h] X-ray Science Division, Advanced Photon Source, Argonne National Laboratory, Argonne, IL 60439, USA
[i] Laboratory for Neutron Scattering and Imaging, Paul Scherrer Institut, CH-5232 Villigen-PSI, Switzerland
[j] Department of Chemistry and Biochemistry, University of Bern, CH-3012 Bern, Switzerland
[k] National High Magnetic Field Laboratory, Los Alamos National Laboratory, Los Alamos, NM 87545, USA

ARTICLE INFO

Article history:
Received 28 September 2019
Accepted 17 January 2020
Available online 22 January 2020

Keywords:
Quantum magnetism
Anisotropy
Low-dimensional
High magnetic fields
Nickel

ABSTRACT

We examine the crystal structures and magnetic properties of several $S = 1$ Ni(II) coordination compounds, molecules and polymers, that include the bridging ligands HF_2^-, AF_6^{2-} (A = Ti, Zr) and pyrazine or non-bridging ligands F^-, SiF_6^{2-}, glycine, H_2O, 1-vinylimidazole, 4-methylpyrazole and 3-hydroxypyridine. Pseudo-octahedral NiN_4F_2, NiN_4O_2 or NiN_4OF cores consist of equatorial Ni-N bonds that are equal to or slightly longer than the axial Ni-L_{ax} bonds. By design, the zero-field splitting (D) is large in these systems and, in the presence of substantial exchange interactions (J), can be difficult to discriminate from magnetometry measurements on powder samples. Thus, we relied on pulsed-field magnetization in those cases and employed electron-spin resonance (ESR) to confirm D when $J \ll D$. The anisotropy of each compound was found to be easy-plane ($D > 0$) and range from $\approx$ 8–25 K. This work reveals a linear correlation between the ratio d(Ni-L_{ax})/d(Ni-N_{eq}) and D although the ligand spectrochemical properties may play an important role. We assert that this relationship allows us to predict the type of magnetocrystalline anisotropy in tailored Ni(II) quantum magnets.

1. Introduction

Low-dimensional magnetism continues to be of great interest to the chemistry and physics communities [1–5]. To a large extent, the resurgence of this field may be attributed to the award of the 2016 Nobel Prize in Physics to Kosterlitz and Thouless for their theoretical work on the *XY* model (also known as easy-plane or planar – i.e., systems exhibiting circular symmetry [6]) and to Haldane for his efforts to realize topological states in integer-spin systems [7]. We are interested in the experimental realization and characterization of these models and how they impact the bulk properties of molecule-based $S = 1$ quantum magnets. In this context, a crucial parameter to be evaluated and, possibly predicted, is the zero-field splitting (ZFS) as it determines the magnetic ground-state of a transition metal ion including that of six-coordinate Ni(II).

For a non-Kramers ion such as $S = 1$ Ni(II), it is known that the sign of the splitting (D) can be positive or negative with the magnitude being 10s of Kelvin [8]. This parameter is particularly sensitive to the symmetry of the coordination sphere and the spin-density distribution of the transition metal and surrounding

* Corresponding authors.
E-mail addresses: jmanson@ewu.edu (J.L. Manson), p.goddard@warwick.ac.uk (P.A. Goddard), john.singleton@physics.ox.ac.uk (J. Singleton).

https://doi.org/10.1016/j.poly.2020.114379
0277-5387/

ligand-field [9]. A combination of experimental probes is generally required to untangle D from the exchange interactions (J) as they tend to be highly correlated when considering bulk data. Thermodynamic measurements such as heat capacity (C_p), high-field magnetization (M), magnetic susceptibility (χ) and inelastic neutron scattering (INS) can be used to assess the ZFS but caution is warranted in the analysis and interpretation of such data obtained for powder samples [10].

If the dominant intrachain/intralayer J is weak relative to D and a field/frequency combination is able to access the relevant excitations, electron-spin resonance (ESR) [11] is the preferred probe for measuring the axial D and rhombic E-terms in the Heisenberg spin Hamiltonian (Eq. (1)).

$$\hat{H} = J\sum_{i,j}\hat{S}_i\cdot\hat{S}_j + J'\sum_{i,j'}\hat{S}_i\cdot\hat{S}_j + D\sum_i\left(\hat{S}_i^z\right)^2 + E\sum_i\left[\left(\hat{S}_i^x\right)^2 - \left(\hat{S}_i^y\right)^2\right] + \mu_B\sum_i B\cdot g\cdot\hat{S}_i \quad (1)$$

In this expression, $\hat{S}$ is the spin operator of each ion (i), $\langle i,j\rangle$ denotes the sum over unique nearest-neighbors, J' is due to interchain/layer interactions and the isotropic Landé g-factor defines the Zeeman energy. Positive J and J' values denote antiferromagnetic (AFM) interactions. For an exchange-free system, the first two terms of the Hamiltonian are negated leaving only the single-ion anisotropy parameters to be determined. The sign of D establishes the preferred orientation of the magnetic moments in a paramagnetic material; i.e. $D > 0$ (XY) and $D < 0$ (Ising; also known as axial or easy-axis). The energy-scale of D can be such that its effects persist well above T_N and compete with thermal fluctuations. For $S = 1$ and the scenario $D > 0$, the ground state is a singlet ($m_s = 0$) and lies below the $m_s = \pm1$ doublet. This means that the Ni(II) magnetic moments prefer a planar orientation perpendicular to the unique axis.

Knowledge of D and its size in proportion to exchange interactions allows a material to be placed on the appropriate phase diagram including, but not limited to, the quasi-1D AFM chain [12]. Unique combinations of these parameters (as well as ancillary couplings J') may lead to new quantum states and theories, as well as permitting access to quantum critical points (QCP) [13].

Molecular materials are particularly well suited for such studies, as the ligand-field and metal-metal spacings may be synthetically manipulated, permitting D and J to be tuned [14]. To this end, we are examining magnetostructural correlations in low-dimensional (zero-, 1- and 2D) $S = 1$ Ni(II) metal–organic quantum systems that contain *trans*-coordinated ligands L situated in pseudo-octahedral NiN_4F_2, NiN_4O_2 or NiN_4OF environments. Equatorial sites consist of N-donor atoms that belong to pyrazine (pyz), glycine (gly), 1-vinylimidazole (vinim), 4-methylpyrazole (mepz) or 3-hydroxypyridine (OHpy). Systematically, it was found that these materials display easy-plane magnetic anisotropy regardless of the structural dimensionality or presence of mild distortion ($E \neq 0$) around the Ni(II) center [15]. For some of these systems, D and J are similar in scale and, in others, $D \gg J$. Herein, we examine these D-J combinations by analyses of X-ray crystal structures and magnetic properties of targeted Ni(II) compounds, molecular and polymeric. We discovered that the experimental D-values linearly track $d(\text{Ni-}L_{ax})/d(\text{Ni-N}_{eq})$ and that this correlation also depends upon the spectrochemical properties of the axial L, which are F^-, HF_2^-, AF_6^- (A = Si, Ti, Zr) or oxygen (from gly or H_2O). Relative to the stronger field amine ligands, stark differences in ligand-field strength and donor-atom electronegativity of L_{ax} leads to D-values up to 25 K. Taken together, this work establishes a predictive strategy to design Ni(II) quantum magnets with $D > 0$.

2. Experimental section

2.1. Syntheses

All chemicals were purchased from commercial suppliers and used without further purification. *CAUTION!* Fluorinated acids, including 48–51% aqueous hydrofluoric acid, are extremely dangerous and must be handled with great care. Appropriate personal protective equipment must be worn even if handling small quantities.

[Ni(HF$_2$)(pyz)$_2$]SbF$_6$ (**1**). As reported in detail elsewhere, aqueous-HF solutions of $NiF_2{\cdot}4H_2O$, NH_4HF_2, $NaSbF_6$ and pyz were slowly mixed to produce a green solution that was covered with perforated Parafilm® [16]. Upon standing at room temperature for ~12 h, a blue micro-crystalline solid began to form on the walls and bottom of the plastic beaker. At this point, the beaker was tightly sealed with a fresh sheet of unperforated Parafilm® and left to stand in a fumehood. After about one year, the solution completely evaporated leaving a large mass of small blue crystals and a few conglomerates of colorless crystals assumed to be NH_4F. The blue crystals were initially characterized by IR spectroscopy followed by laboratory-based single crystal X-ray diffraction which confirmed the material to be **1**. The extremely slow solvent evaporation proved imperative in producing crystals of suitable size for the X-ray study.

NiF$_2$(pyz)$_2{\cdot}3H_2O$ (**2**). $NiF_2{\cdot}4H_2O$ (0.3503 g, 2.07 mmol) was dissolved in 2-mL of aqueous HF (48–51% by volume) and slowly poured into a 10-mL aqueous solution containing a large excess of pyz (3.3157 g, 41.40 mmol). A blue solution formed immediately with no precipitate. The reaction mixture was stirred for an additional 30 min, covered with perforated Parafilm® and left to stand at room temperature in the fumehood. After one-day, a small amount of pale blue precipitate was observed. Upon standing for another 7 days, the precipitate became darker blue with much more material forming on the walls and bottom of the plastic beaker. The solid was scraped off of the beaker, filtered using vacuum filtration and washed with 10-mL of fresh H_2O. As a final wash, 10-mL of EtOH and 20-mL of Et_2O were used successively to assist in drying the sample. The obtained product had a mass of 0.3643 g (57% yield) and was pale blue-gray in color.

[Ni(gly)$_2$(pyz)]·5.21H$_2$O (**3**). While stirring, neat glycine (0.6324 g, 8.40 mmol) was added to a 20-mL hot aqueous suspension of $NiCO_3$ (0.5010 g, 4.21 mmol). To this teal colored solution was added neat pyrazine (0.3364 g, 4.20 mmol). Upon slow solvent evaporation overnight, a large mass of light brown needles formed on the walls and bottom of the beaker. The crystals were collected by vacuum filtration and lightly dried. Upon careful inspection a few small blue crystals, identified by X-ray diffraction as $Ni(gly)_2(H_2O)_2$ [17], were found and mechanically separated. The total collected mass of product was 0.9089 g (57% yield) based on Ni ion.

Ni(AF$_6$)(vinim)$_4$ (A = Ti, **4a** and **4b**; A = Zr, **5**). $Ni(NO_3)_2{\cdot}6H_2O$ (0.2004 g, 0.69 mmol) was dissolved in 3-mL of H_2O and mixed with a 5-mL aqueous solution containing $(NH_4)_2TiF_6$ (0.1682 g, 0.85 mmol) and vinim (0.2861 g, 3.04 mmol). While stirring, a pale blue precipitate (**4a**) formed immediately which was collected by vacuum filtration, washed with 2-mL H_2O, followed by 2-mL EtOH and dried *in vacuo*. Small blue-purple prisms (**4b**) suitable for X-ray diffraction were grown by slow evaporation of dilute 1:1 aqueous EtOH solutions. $Ni(ZrF_6)(vinim)_4$ (**5**) was synthesized in a similar manner but replacing $(NH_4)_2TiF_6$ with $(NH_4)_2ZrF_6$. Typical product yields of **4a**, **4b** and **5** were 25–35% based on vinim.

[Ni(SiF$_6$)(mepz)$_4$(H$_2$O)]·H$_2$O (**6**). $NiSiF_6{\cdot}6H_2O$ (0.4500 g, 1.46 mmol) was dissolved in 2-mL of water and added dropwise to a 20-mL EtOH solution containing 4-methylpyrazole (0.4795 g, 5.64 mmol) to produce a teal colored solution. The reaction mix-

ture was covered with Al-foil and left to stand undisturbed at room temperature. After about 2 hrs, a green precipitate formed which was removed by vacuum filtration. The mother liquor remained teal in color and was again set aside to slowly evaporate. Upon standing for approximately 18 h, a large mass of deep blue crystals formed. These were collected by vacuum filtration and gently air-dried for about 30 min. The crystalline product was obtained in 54% yield (0.4434 g) based on mepz.

$NiF_2(OHpy)_4$ (**7**). A 10-mL aqueous solution containing dissolved $Ni(NO_3)_2{\cdot}6H_2O$ (0.2010 g, 0.69 mmol) was slowly added to a 40-mL 50:50 H_2O/EtOH solution containing NH_4HF_2 (0.0981 g, 1.72 mmol) and four equivalents of 3-hydroxypyridine (0.2653 g, 2.76 mmol). A pale green solution formed immediately with no precipitate. The beaker was covered with perforated Al-foil and left to stand at room temperature. After several minutes, a gray-green precipitate began to form. The reaction was allowed to continue overnight and the solid collected by suction filtration. Aliquots of 2-mL H_2O followed by 2-mL EtOH were used to wash the solid which was then dried *in vacuo* for 3 h. The material was obtained in 72% yield (0.2370 g) based on Ni(II) content. Crystals suitable for the X-ray diffraction study were recovered from the final product.

2.2. Single crystal X-ray diffraction

Suitable crystals were selected from the bulk, mounted on a cryo-loop and cooled to 100 K using a LN2 cryostream. X-ray data were collected on a Bruker D8 Venture CPAD DUO micro-source diffractometer using ϕ and ω scans with graphite mono-chromatic Mo*Ka* (λ = 0.71073 Å) radiation. Data sets were corrected for Lorentz and polarization effects as well as absorption. The criterion for observed reflections was $I > 2\sigma(I)$. Lattice parameters were determined from least-squares analysis of reflection data. Empirical absorption corrections were applied using SADABS [18]. Structures were solved by direct methods and refined by full-matrix least-squares analysis on F^2 using the SHELXT [19] functionality within X-SEED [20]. Non-hydrogen atoms were refined anisotropically using the SHELXL program [21]. Hydrogen atoms (for OH and NH) were located by difference Fourier synthesis and refined isotropically with independent O/N-H distances or restrained to 0.85(2) Å. Remaining H-atoms were placed in idealized geometric positions with U_{iso} = 1.2U_{eq} of the atom to which they were attached; U_{iso} = 1.5U_{eq} for methyl groups. Tables 1 and 2 list structural and refinement parameters.

2.3. Synchrotron X-ray powder diffraction

High-resolution data were collected using beamline I11 located at the Diamond Light Source Ltd, Didcot, UK [22] and beamline 11-BM at the Advanced Photon Source, Argonne National Laboratory [23]. Samples of **2** (11-BM) and **4a** (I11) were prepared in 0.5-mm Kapton or borosilicate capillaries, respectively, and measured in transmission geometry. I11 used a position sensitive Mythen detector while discrete detectors were scanned over a 34° range in 2θ with data points collected every 0.001° on 11-BM. Data for **2** were collected only at room temperature whereas **4a** was cooled to 100 K using a LN2 cryostream. Structural refinements were carried out using FULLPROF [24].

2.4. SQUID magnetometry

Linear susceptibility (χ = M/H) measurements were made for temperatures in the range $1.9 \leq T \leq 300$ K and fields $\mu_0 H \leq 7$ T using a Quantum Design Magnetic Property Measurement System (MPMS) equipped with a standard dc transport. Powder samples with masses of 2–5 mg were packed in gelatin capsules, loaded in a plastic drinking straw, affixed to the end of a stainless steel/brass rod, and mounted on the transport. Samples were cooled in zero magnetic field to 1.9 K, the field charged to 0.1 T and data taken upon warming.

2.5. Pulsed-field magnetization

Measurements on each sample were made up to 60 T using a 1.5 mm bore, 1.5 mm long, 1500-turn compensated-coil susceptometer constructed from a 50 gauge high-purity copper wire [25]. When the sample is within the coil, the signal voltage V is proportional to dM/dt, where t is time. Numerical integration of V is used to evaluate M. The sample is mounted within a 1.3 mm diameter

Table 1
X-ray structural and refinement parameters for $[Ni(HF_2)(pyz)_2]SbF_6$ (**1**), $NiF_2(pyz)_2{\cdot}3H_2O$ (**2**), $[Ni(gly)_2(pyz)]{\cdot}5.21H_2O$ (**3**), $[Ni(SiF_6)(mepz)_4(H_2O)]{\cdot}H_2O$ (**6**) and $NiF_2(OHpy)_4$ (**7**).

Compound	**1**	**2**	**3**	**6**	**7**
Instrument	Bruker D8	APS 11-BM	Bruker D8	Bruker D8	Bruker D8
Method	single crystal	powder	single crystal	single crystal	single crystal
T (K)	100	297	100	100	100
λ (Å)	0.71073	0.41334	0.71073	0.71073	0.71073
Emp. formula	$C_8H_9F_8N_4NiSb$	$C_8H_{11}F_5N_4Ni$	$C_8H_{21.92}N_4NiO_{9.21}$	$C_{16}H_{28}F_6N_8NiO_2Si$	$C_{20}H_{20}F_2N_4NiO_4$
MW (g mol^{-1})	493.65	310.91	380.33	565.26	477.11
Crystal class	tetragonal	monoclinic	monoclinic	monoclinic	orthorhombic
Space group	*P*4/*nmm*	*I*2/*m*	*C*2/*c*	*Cc*	*Pccn*
a (Å)	9.8946(4)	6.67443(1)	34.287(6)	12.7840(6)	7.3520(2)
b (Å)	9.8946(4)	10.2458(1)	6.980(1)	14.2862(6)	14.6066(4)
c (Å)	6.4292(3)	8.75067(2)	13.395(2)	13.5967(6)	17.9448(6)
α (°)	90	90	90	90	90
β (°)	90	104.261(1)	107.498(6)	99.963(2)	90
γ (°)	90	90	90	90	90
V (Å^3)	629.44(6)	579.977(2)	3057.2(8)	2445.8(2)	1927.1(1)
Z	2	2	8	4	4
ρ_{exp} (g cm^{-3})	2.605	1.815	1.653	1.535	1.644
μ (mm^{-1})	3.742	—	1.322	0.918	1.064
No. meas. refs.	6060	2729	10,899	25,801	32,005
No. uniq. refs.	378	—	3127	4806	1977
No. params.	36	93	257	344	147
GOF or χ^2	1.107	4.510	1.071	1.047	1.110
R_1	0.0113	0.0611	0.0580	0.0253	0.0260
wR_2	0.0292	0.0904	0.1392	0.0556	0.0659
$\Delta\rho$ −/+ (e Å^{-3})	−0.453, 0.348	—	−0.727, 1.292	−0.218, 0.254	−0.389, 0.297

Table 2
X-ray structural and refinement parameters for $Ni(TiF_6)(vinim)_4$ (**4a** and **4b**) and $Ni(ZrF_6)(vinim)_4$ (**5**).

Compound	4a	4b	5
Instrument	Diamond I11	Bruker D8	Bruker D8
Method	powder	single crystal	single crystal
T (K)	100	100	100
λ (Å)	0.82460	0.71073	0.71037
Emp. formula	$C_{20}H_{24}F_6N_8NiTi$	$C_{20}H_{24}F_6N_8NiTi$	$C_{20}H_{24}F_6N_8NiZr$
MW (g mol^{-1})	597.01	597.01	640.37
Crystal class	tetragonal	tetragonal	tetragonal
Space group	$P4_2/n$	$I4/m$	$P4_2/n$
a (Å)	12.45777(2)	12.4718(5)	12.4859(11)
b (Å)	12.45777(2)	12.4718(5)	12.4859(11)
c (Å)	7.89890(2)	7.9087(3)	8.1946(7)
α (°)	90	90	90
β (°)	90	90	90
γ (°)	90	90	90
V (Å^3)	1225.877(4)	1230.17(8)	1277.5(3)
Z	2	2	2
ρ_{exp} (g cm^{-3})	1.618	1.601	1.665
μ (mm^{-1})	—	1.161	1.213
No. meas. refs.	3557	4368	7298
No. uniq. refs.	—	895	1580
No. params.	74	77	82
GOF or χ^2	164.76	1.060	1.040
R_1	0.0237	0.0189	0.0211
wR_2	0.0379	0.0482	0.0491
$\Delta\rho$ −/+ (e Å^{-3})	—	−0.339, 0.387	−0.347, 0.322

ampoule that can be moved in and out of the coil. Accurate values of M were obtained by subtracting empty-coil data from that measured under identical conditions with the sample present. The susceptometer was placed inside a ^{3}He cryostat providing a base temperature of 0.5 K. The magnetic field was measured by integrating V induced in a 10-turn coil calibrated by observing the de Haas-van Alphen oscillations of the belly orbits of the copper wires in the susceptometer coil [25].

2.6. Electron-spin resonance

High-field, high-frequency ESR spectra of powdered samples at temperatures ranging from ≈ 3 to 20 K were recorded on a home-built spectrometer at the EMR facility of the National High Magnetic Field Laboratory using microwave frequencies 52–626 GHz. The instrument is a transmission-type device and uses no resonant cavity. The microwaves were generated by a phase-locked Virginia Diodes source, generating frequency of 13 ± 1 GHz, and equipped with a cascade of frequency multipliers to generate higher harmonics. A superconducting magnet (Oxford Instruments) capable of reaching a field of 17 T was employed.

2.7. Muon-spin relaxation

Zero-field muon-spin relaxation (μ^+SR) studies [26] were carried out on a powder sample of **2** using the General Purpose Surface-Muon (GPS) spectrometer located at the Swiss Muon Source (SμS), Paul Scherrer Institute, Switzerland. The sample was wrapped in 25-μm Ag foil and mounted on a Cu fork using aluminized Mylar tape. Sample cooling was achieved using a side-loading continuous-flow ^{4}He cryostat.

2.8. Electronic structure calculations

Computational modeling was executed on dinuclear moieties using the structural data from X-ray determinations. Evaluation of the exchange couplings was based on the broken-symmetry (BS) approach of Noodleman [27] as implemented in the ORCA version 4.1.1. suite of programs [28,29]. The formalism of Yamaguchi, which employs calculated expectation values $\langle S^2 \rangle$ for both high-spin and broken-symmetry states was used [30]. Auxiliary fitting bases were generated with the AutoAux procedure of ORCA [31]. Calculations related to magnetic interactions were performed using the PBE0 functional. The scalar relativistically recontracted version of the Aldrichs triple-ζ basis set, def2-TZVP, was used for all atoms [32]. Numerical integrations for all DFT calculations were implemented using dense grids.

The ZFS were modeled by a complete active space self-consistent-field (CASSCF) approach employing the scalar relativistically recontracted basis sets tailored for use with the Douglas-Kroll-Hess (DKH) Hamiltonian. The basis sets were of triple-ζ quality for all atoms (DKH-def2-TZVP) except for Zr where DKH-TZVP was employed within ORCA. In all calculations, the second order DKH Hamiltonian was used. For all systems, minimalistic, monomeric models based on the experimental geometries were used and the active space limited to the Ni d-orbitals.

3. Results and discussion

3.1. Structural and magnetic properties of a model S = 1 XY system $[Ni(HF_2)(pyz)_2]SbF_6$ (**1**)

Our interest in **1** was motivated by the desire to quantify two key parameters: (*i*) the exchange coupling (J) along the strong hydrogen bonded Ni-FHF-Ni pathway and (*ii*) the potentially large D of the Ni(II) ion involved in NiN_4F_2 coordination. Initial difficulty in growing suitable single crystals limited experiments to powders and relied on high-magnetic field and neutron scattering techniques to untangle the D and J values [33]. A 3D XY magnetic ground-state was revealed wherein D and J are quantitatively similar. Using **1** as a prototype, we briefly review its magnetic properties to give context to the current work. Herein, new theoretical results on **1** are presented as well as the X-ray crystal structures and magnetic properties of several new molecule-based Ni(II) systems that also display large easy-plane anisotropy (see Table 3).

3.1.1. Crystal structure at 100 K

$[Ni(HF_2)(pyz)_2]SbF_6$ (**1**)Crystallizes in the tetragonal space group $P4/nmm$ (S. G. #129) with $Z = 2$. Nearly isotropic NiN_4F_2 octahedra (Fig. 1a) consist of two axially-ligated F-atoms belonging to HF_2^- ions [d(Ni-F1) = 2.074(2) Å] while the equatorial plane contains four pyz ligands coordinated through N-donor atoms [d(Ni-N1) = 2.101(2) Å]. The Ni(II) center lies on a $\bar{4}2m$ site leading to a propeller-like disposition of the pyz rings which make a dihedral angle of 72.9(1)° with-respect-to the ab-plane. A 3D MOF-like framework of composition $[Ni(HF_2)(pyz)_2]^+$ is formed owing to the bridging nature of the HF_2^- and pyz ligands (Fig. 1b). Linear 1D Ni-FHF-Ni chains (n = 2) propagate along the c-axis with d (Ni···Ni) separations of 6.4292(3) Å. These chains are cross-linked by pyz ligands to afford $[Ni(pyz)_2]^{2+}$ square sheets with d (Ni···Ni) = 6.9965(4) Å. Thus, each Ni-FHF-Ni chain is equidistant to four identical nearest-neighboring chains (n' = 4). Voids within the framework are occupied by SbF_6^- counterions.

From Fig. 1b it can be seen that two distinct types of hydrogen bonds exist; those internal to the HF_2^- ligand [d(H1···F1) = 1.141(2) Å; F···H···F = 180°] and those mediated between pyz H-atoms and interstitial SbF_6^- anions via weaker C1-H1A···F4 interactions [d(H1···F4) = 2.490(2) Å; C-H···F = 147.1(2)°]. We suggest that the latter H-bond type restricts positional disorder of the pyz rings common to other tetragonal systems such as $NiX_2(pyz)_2$ (X = Cl, Br, I, NCO) [34,35]. The X = F material (see below) has monoclinic symmetry and does not exhibit pyz ring disorder.

Table 3
Comparison of Ni-ligand bond lengths and key magnetic parameters for $[Ni(HF_2)(pyz)_2]SbF_6$ (**1**), $NiF_2(pyz)_2{\cdot}3H_2O$ (**2**), $[Ni(gly)_2(pyz)]{\cdot}5.21H_2O$ (**3**), $Ni(TiF_6)(vinim)_4$ (**4a** and **4b**), $Ni(ZrF_6)(vinim)_4$ (**5**), $[Ni(SiF_6)(mepz)_4(H_2O)]{\cdot}H_2O$ (**6**) and $NiF_2(OHpy)_4$ (**7**). Experimental values for J, $\mu_0H^x_{sat}$ and $\mu_0H^z_{sat}$ were determined from plots of dM/dH except where indicated. g-factors are reported for ESR data.

Compound	**1**	**2**	**3**	**4a**	**4b**	**5**	**6**	**7**
S. G.	*P*4/*nmm*	*I*2/*m*	*C*2/*c*	$P4_2/n$	*I*4/*m*	$P4_2/n$	*Cc*	*Pccn*
Ni-N (Å)	2.101(2)	2.117(2)	2.097(4)	2.005(4)	2.070(1)	2.078(1)	2.085(3)[£]	2.107(2)[£]
Ni-*L* (Å)	2.074(2)	2.004(2)	2.059(3)	2.076(3)	2.072(1)	2.078(1)	2.063(2)[§]	2.055(2)
d(Ni-N)-*d*(Ni-*L*)	0.027	0.113	0.038	−0.071	−0.002	0.000	0.022	0.052
g_x	—	—	—	—	—	—	2.240(7)	2.2205(4)
g_y	—	—	—	—	—	—	2.228(5)	2.220(3)
g_z	—	—	—	2.2(2)	—	2.22(1)	2.158(5)	2.151(4)
$D_{\chi(T)}$ (K)	11.8	—	—	24.9(1)	—	18.5(1)	11.25(2)	12.3(5)
$E_{\chi(T)}$ (K)	0	—	—	0	—	0	0.6(1)	1.9(1)
$\sqrt{D^2 - E^2}$ (K)*	13.3(1), 15(1)[¥]	8.0(5)	8.0(6)	—	—	—	11.8(7)	12.2(3)
D_{ESR} (K)	—	—	—	23.8(5)	—	20.0(5)	11.45(2)	12.36(1)
E_{ESR} (K)	—	—	—	0	—	0	0.49(1)	1.16(1)
J (K)	10.4(1), 10.7(1)[¥]	0.49(2)	0.7(2)	≈0	—	≈0	≈0	≈0
$\mu_0H^x_{sat}$ (T)	32.0(3)	5.1(1)	1.8(2)	—	—	—	—	—
$\mu_0H^z_{sat}$ (T)	54(1)	15.5(3)	12.5(5)	—	—	—	7.8(6)	8.4(2)

[£] average Ni-N bond length.
[§] shortest of the two Ni-*L* distances.
[¥] obtained by independent simulation of $\chi(T)$, $M(H)$ and inelastic neutron scattering data (see Ref [33]).
* Determined from $M(H)$ data; for tetragonal systems, $E = 0$ so $M(H)$ gives D directly in those cases.

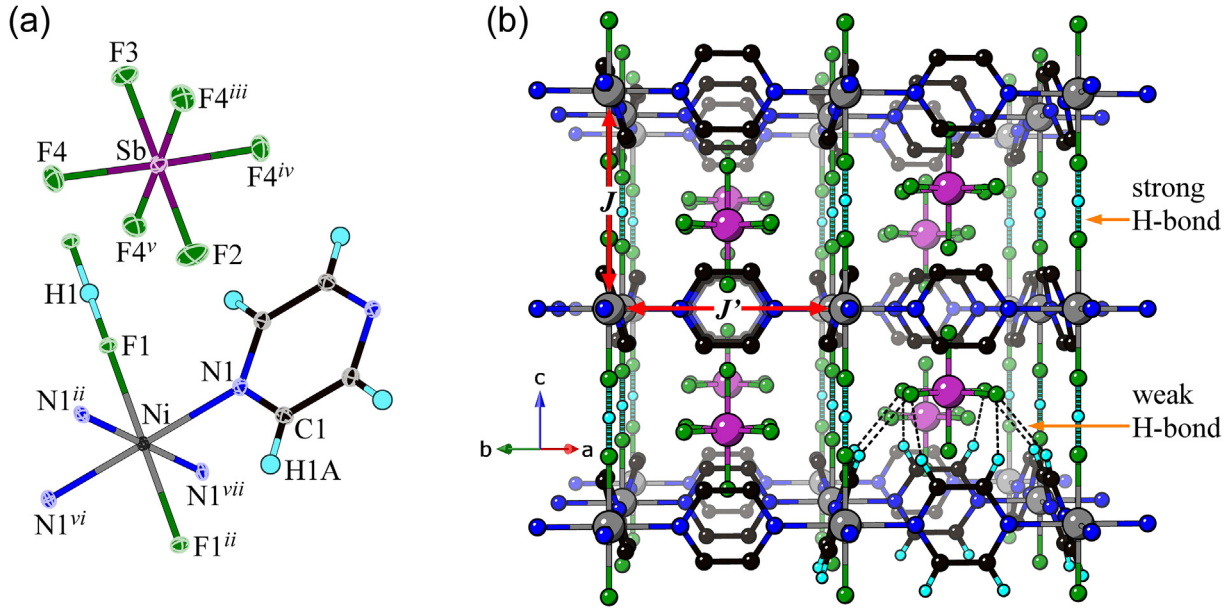

Fig. 1. Single crystal X-ray structure of $[Ni(HF_2)(pyz)_2]SbF_6$ (**1**) determined at $T = 100$ K. (a) Thermal ellipsoid plot (40% probability level) and atom labeling scheme. The Ni(II) center has local D_{4h} symmetry. Symmetry codes: (*ii*) ($y - 1/2, -x + 1, -z$); (*iii*) ($-y + 1/2, x, z$); (*iv*) ($-x + 1/2, -y + 1/2, z$); (*v*) ($y, -x + 1/2, z$); (*vi*) ($-x + 1/2, -y + 3/2, z$); (*vii*) ($-y + 1, x + 1/2, -z$). (b) Polymeric 3D MOF-like structure. For simplicity, only the lower right quadrant shows the 'nested' C-H···F hydrogen bonds that tether the SbF_6^- counterion in place.

3.1.2. Previously reported magnetic properties [33]

High-field $M(H)$ data were measured up to 60 T for a powder sample at several temperatures above and below $T_N = 12.2$ K, the latter being established by $C_p(T)$ and neutron diffraction. A slightly concave $M(H)$ curve and broad approach to saturation were observed (Fig. 2a), signifying low-dimensional AFM spin correlations and the presence of a large D-value, respectively. Within the easy-plane model, $g\mu_B\mu_0H^x_{sat} = 2S\langle J\rangle$ is the point at which the Ni(II) moments saturate for fields lying in the easy-plane, while $g\mu_B\mu_0H^z_{sat} = 2S(n\langle J\rangle + D)$ is for fields parallel to the hard-axis [33]. Here, n is the total number of effective nearest-neighbor exchange pathways and $\langle J\rangle$ is the average exchange strength. The D-value and $n\langle J\rangle$ were initially parameterized by finding the two critical fields [$\mu_0H^x_{sat} = 32.0(3)$ T and $\mu_0H^z_{sat} = 54(1)$ T] from a plot of dM/dH vs. μ_0H. Applying mean-field theory and assuming Heisenberg behavior for the Ni(II) ion, we found $D = 15(1)$ K and $n\langle J\rangle = 22.4(2)$ K.

The $M(H)$ data were successfully simulated using a Monte-Carlo algorithm based on an eight-spin cluster and complete powder-averaging for numerous spin orientations, yielding the following parameters: $D = 13.3$ K, $J = 10.4$ K, $J' = 1.4$ K (solid line in Fig. 2a). Intra- (J) and interchain (J') magnetic couplings are assigned to the respective Ni-FHF-Ni and Ni-pyz-Ni pathways. The small J' of ≈ 1–2 K is typical of the exchange interaction encountered in several Ni(II)-pyz coordination polymers [10,33–35].

Inelastic neutron scattering (INS) measurements were made on a powder sample using a cold-neutron disk-chopper spectrometer. Subtracting data obtained in the paramagnetic state (20 K) from data obtained for $T \ll T_N$ (1.5 K) revealed a clear magnetic excitation centered at $S(Q,\omega) \approx 3.4$ meV ≈ 39.4 K (Fig. 2b). As this

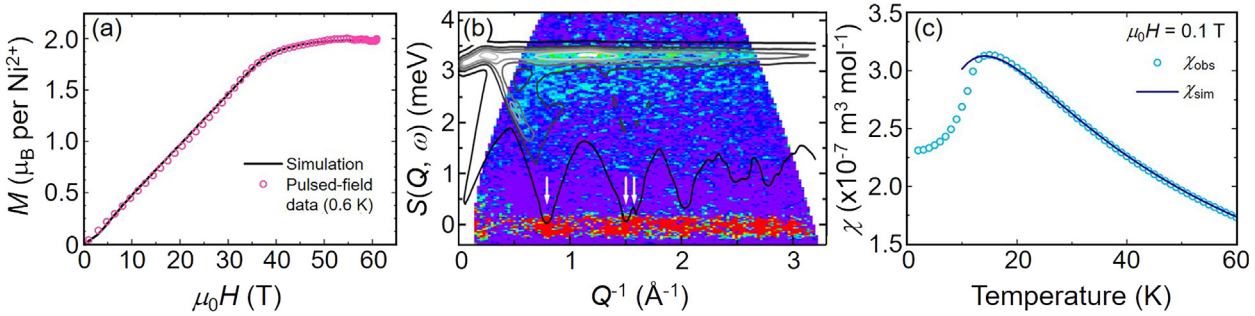

Fig. 2. (a) $M(H)$ and (b) INS data for powder samples of **1**. The simulated traces in (a) and (b) coincide with D = 13.3(1) K, J = 10.4(3) K and J' = 1.4(2) K as described in the text. White arrows in (b) indicate magnetic Bragg peaks arising from the 3D *XY*-ordered magnetic ground-state. (c) Experimental $\chi(T)$ along with the theoretical curve obtained for D = 11.8 K, J = 10.7 K and J' = 0. See ref. [33] for details.

excitation disappears above T_N it must originate from spin-waves meaning that the total energy results from the sum of all magnetic contributions such that $S(Q,\omega) \approx D + 2J + 4J'$. Simulating the spin-wave features (overlay plot in Fig. 2b), taking into account energy and wave-vector transfers, affords very good agreement for the parameters: D = 13.3(1) K, J = 10.4(3) K and J' = 1.4(2) K, in keeping with thermodynamic measurements [33].

For $k_BT < D$, the positive-D value dictates an *XY* spin configuration of the Ni(II) magnetic moments within the *ab*-plane; i.e., normal to the Ni-FHF-Ni chains. Below T_N = 12.2(1) K, the Ni moments adopt a collinear, 3D *XY*-AFM ordered ground-state as confirmed by symmetry analyses of neutron diffraction data [33]. At 1.5 K, a refined ordered moment of 2.03(7) μ_B was found as is typical of an ion containing two unpaired electrons. A fit of the order parameter gives a β-value of 0.141(1) which is consistent with a low-dimensional AFM magnetic structure.

Magnetic susceptibility [33] data obtained for a powder sample of **1** shows a broad maximum at 16 K and a subtle kink at ≈ 12 K. The former features arise from short-range correlations along the Ni-FHF-Ni chains and the latter from long-range magnetic order between them. As no theoretical model exists to fit $\chi(T)$ for coupled S = 1 chains where D and J are of similar scale, we simulated these data (Fig. 2c) to arrive at D = 11.8 K, J = 10.7 K and J' = 0 for the best values. The combination of experimental probes was necessary owing to the ambiguity in fitting the $\chi(T)$ derived from powder data with three variables D, J and J'.

3.1.3. Electronic structure calculations

The spin-density distribution, exchange constants [33] and ZFS have been computed for **1**. It was previously shown that a portion of the Ni(II) magnetic moment (≈ 0.2*e*) was equally delocalized onto the F- and N-donor atoms. However, the close proximity of F-atoms within HF_2^- provides nearly direct p_z-p_z orbital overlap which leads to more effective spin exchange along Ni-FHF-Ni. The *N*-atoms of the pyz ring contain the bulk of the spin-density in the NiN_4 equatorial plane with only minute spin-density on the C-atoms [33]. This reduces the overall ability of pyz to efficiently mediate magnetic exchange along Ni-pyz-Ni, in contrast to the many Cu(II)-pyz variants [36–41].

Using CASSCF, the ZFS (this work) of the Ni(II) ion in **1** was computed for an uncharged mononuclear fragment $[Ni(HF_2)_2(pyz)_4]$, ignoring counterions, but retaining the experimentally determined coordination geometry. The resulting ZFS-tensor was found to be diagonal in the Cartesian frame of the ligators and perfectly axial: D = 16.9 K and E/D = 0. By comparison, the calculated D is consistent with the experimental $M(H)$ and INS values. The E/D value should be strictly zero for a tetragonal system.

3.2. Structural and magnetic properties of $NiF_2(pyz)_2{\cdot}3H_2O$ (**2**)

3.2.1. Crystal structure at 297 K

The difficulty in growing single crystals of (**2**) for X-ray diffraction required implementation of X-ray powder methods (Fig. 3) to determine and refine the crystal structure of **2**. Unlike the tetragonal members in the $NiX_2(pyz)_2$ series (X = Cl, Br, I) [34] the crystal structure of X = F is monoclinic ($I2/m$). Pyrazine ligands link adjacent Ni(II) ions into square lattices (Fig. 4a) with d(Ni···Ni) = 7.024 (1) Å and propagate along the (1 0 –1)-direction. Inversion centers occupy the center of each square and mirror planes (confined to the *ac*-plane) pass through Ni(II) ions located on opposite corners of the square. Glide planes run parallel to these mirrors and contain the midpoints of the pyz ligands.

Compressed NiN_4F_2 octahedra are composed of four equal d(Ni-N1) bonds of 2.117(2) Å and two axially-ligated F-atoms [d(Ni-F1) = 2.004(2) Å]. Angular distortion around the Ni(II) center is small with F1-Ni-N1 being 90.3(1)°. Two-fold rotational symmetry about the F1-Ni-F1 axis negates the propeller-like disposition of pyz ligands observed in **1** [33,36]. This implies that for both Ni-pyz-Ni directions, the pyz ligands retain the same spatial arrangement and do not alternately tilt, a feature common in 1D chains such as $[Ni(gly)_2(pyz)]{\cdot}5.21H_2O$ (**3**) but rare in 2D lattices. Each pyz is tilted away from the NiN_4 plane by 67.3(1)°. The trajectory of the Ni-pyz interaction is somewhat non-linear as indicated by Ni-N1···N1^{vii} [175.6(1)°] which may limit efficiency of the magnetic exchange interaction (see below).

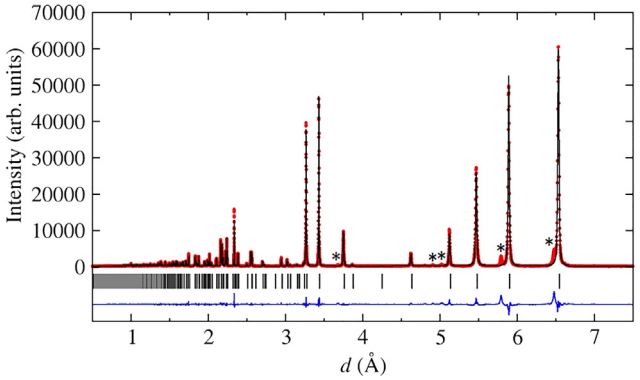

Fig. 3. T = 297 K X-ray powder diffraction data (●) for **2** along with the Rietveld refinement (—). Short vertical lines indicate expected Bragg positions whereas the difference plot ($I_{obs} - I_{calc}$) is shown as the blue line at the bottom. A handful of minor Bragg peaks belong to an unidentified impurity phase (*). (For interpretation of the references to colour in this figure legend, the reader is referred to the web version of this article.)

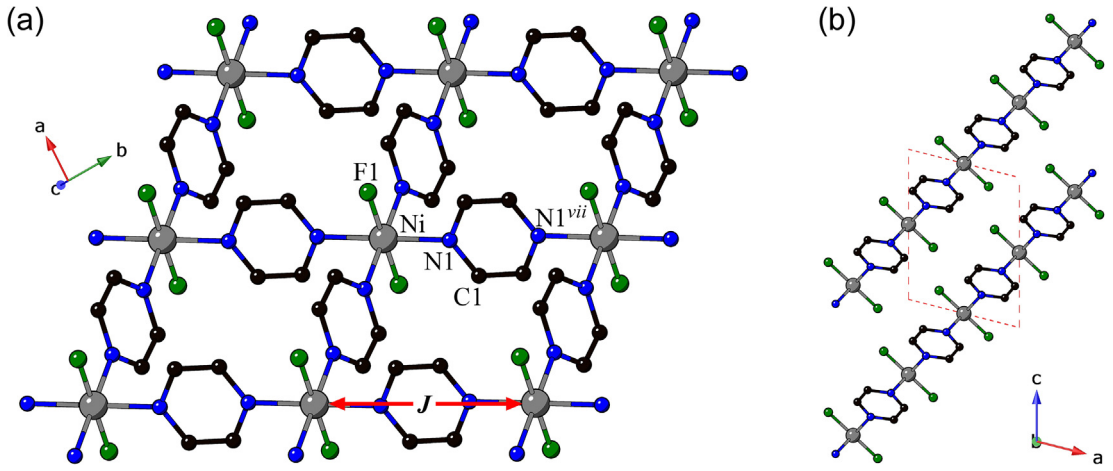

Fig. 4. (a) Crystal structure of $NiF_2(pyz)_2{\cdot}3H_2O$ (**2**) showing a portion of an infinite 2D square lattice with pyz H-atoms and H_2O molecules omitted for clarity. Symmetry code: (*vii*) $(-x + 1/2, -y + 1/2, -z + 1/2)$. Pyz ligands adopt identical configurations along the Ni-pyz-Ni axes which contrasts with **1** where pyz ligands alternately rotate along these segments. (b) Layer packing in **2** with the unit cell depicted as red dashes. (For interpretation of the references to colour in this figure legend, the reader is referred to the web version of this article.)

Adjacent layers alternately pack in a staggered fashion in the direction normal to the F-Ni-F axis (Fig. 4b). This gives the closest interlayer *d*(Ni···Ni) separation of 6.6744(1) Å which coincides with the *a*-axis unit cell dimension. Interstitial sites are occupied by HF or H_2O solvent molecules for which only the heavy atoms could be located during Rietveld refinement. The heavy atom distance of 2.436(2) Å is consistent with either *d*(O···O) (typical range 2.363–2.46 Å; median = 2.413 Å) [42] or *d*(F···F) (2.32–2.497 Å; median = 2.457 Å) as reported for several poly-HF adducts [42]. The final structural refinement for **2** settled on H_2O although the material may contain a mixture of HF/H_2O molecules, perhaps partially occupied (see Figs. S1 and S2), and this could slightly affect quantitative interpretation of the magnetometry data.

3.2.2. Magnetic susceptibility

The temperature-dependence of the magnetic susceptibility is presented in Fig. 5a. Upon cooling to 1.8 K, a rounded maximum was observed at 4.3 K with a subtle kink occurring near 2.3 K that may arise from long-range magnetic order (see below). At base temperature, the minimum value of $\chi(T)$ is 0.085 $cm^3\ mol^{-1}$. In the inset of Fig. 5a, a Curie-Weiss fit of $1/\chi(T)$ reveals linear behavior over the range $50 \leq T \leq 300$ K from which the *g*-factor of 2.28 (1) and θ_{CW} = -3.9(6) K were determined. The *g*-factor is typical of Ni(II) ions in this environment [8] and the negative Weiss constant indicates AFM coupling between the Ni(II) ions, likely within the square lattice. It is important to note that powder $\chi(T)$ data like these can be fitted equally well to several models containing only anisotropy terms or only exchange terms, but choosing one such

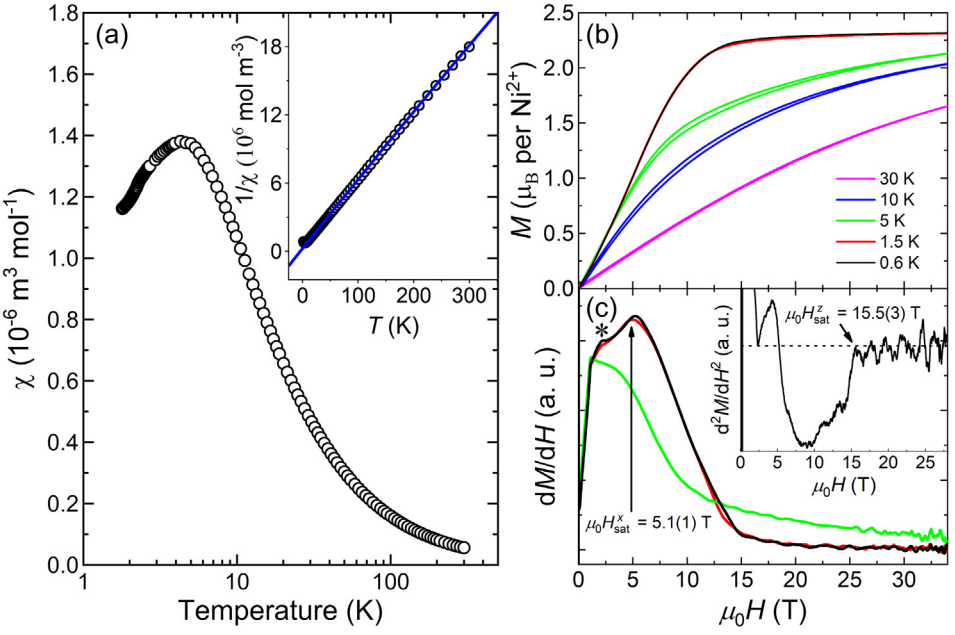

Fig. 5. Magnetometry data for powdered **2**. (a) Zero-field cooled $\chi(T)$ measured at μ_0H = 0.1 T. Inset shows $1/\chi(T)$ (circles) fit to a Curie-Weiss model (line) for $50 \leq T \leq 300$ K. (b) Pulsed-field magnetization calibrated using DC-field SQUID magnetometry. (c) dM/dH shows two saturation fields $\mu_0H^x_{sat}$ and $\mu_0H^z_{sat}$ for fields applied parallel and perpendicular to the easy direction. Another unidentified feature is labelled with an asterisk and discussed in the text. Inset shows d^2M/dH^2 used to determine $\mu_0H^z_{sat}$. The dashed line corresponds to $d^2M/dH^2 = 0$.

model leads to erroneous conclusions in the case where both D and J are present. An effective 2D fitting function of the susceptibility for an S = 1 Hamiltonian containing both D and J does not exist. With this limitation, we computed J for **2** using DFT and found a value of 5.4 K which exceeds the typical upper limit of ≈ 1–2 K expected for Ni-pyz-Ni pathways [10,33–35].

3.2.3. Pulsed-field magnetization

Pulsed-field magnetization $M(H)$ (calibrated using DC-field SQUID data) are shown in Fig. 5b. At the lowest temperatures, the measured $M(H)$ shows a slightly curved rise to a broad saturation, indicative of an S = 1 antiferromagnet with single-ion anisotropy. The saturation magnetization value of 2.32(6) μ_B per Ni^{2+} ion is in good agreement with the g-factor determined from the susceptibility data.

Differential susceptibility (dM/dH) data (Fig. 5c) exhibits two characteristic fields, as expected for a polycrystalline measurement. Defining $\mu_0 H^x_{sat}$ = 5.1(1) T as the field at which dM/dH begins to drop, and $\mu_0 H^z_{sat}$ = 15.5(3) T as the point at which d^2M/dH^2 tends to zero, we find that $n\langle J\rangle$ = 1.95(4) K and D = 8.0(5) K. However, the local Ni(II) site symmetry suggests a small E-term is possible. Assuming negligible interplane exchange coupling, n = 4 and $\langle J\rangle = J_{pyz}$ = 0.49(2) K, which is similar to the Ni-pyz-Ni exchange energies found in several other square $[Ni(pyz)_2]^{2+}$ motifs [10,33–35].

As shown by an asterisk in Fig. 5c, an additional small feature is observed in the pulsed-field dM/dH data at the lowest temperatures. The feature is not consistent with the spin-flop field estimated using the two observed saturation fields within an easy-axis model. However, analogous behavior was observed in $[Ni(H_2O)_2(pyz)_2](BF_4)_2$ wherein neutron diffraction data confirmed a XY magnetic ground-state with Ni(II) moments confined to the $[Ni(pyz)_2]^{2+}$ square lattice [10].

3.2.4. Muon-spin relaxation

μ^+SR asymmetry spectra of **2** collected in zero applied magnetic field are shown in Fig. 6a for temperatures of 1.7 K and 3.1 K. The spectrum at 1.7 K shows rapid oscillations that indicate long-range magnetic order [26]. No oscillations were seen in the 3.1 K data, suggesting that the magnetic order is destroyed by this temperature. We fit this data to the model shown in Eq. (2),

$$A(t) = A_1 e^{-\lambda_1 t}\cos\left(\gamma_\mu B t + \varphi\right) + A_2 e^{-\lambda_T t} + A_3 e^{-\lambda_B t} \quad (2)$$

Here, A_1 = 0.062, A_2 = 0.045, and A_3 = 0.097 are the temperature independent asymmetries of the three components, λ_1, λ_T, and λ_B are their relaxation rates, B is the internal field, γ_μ = 2π x 135.5 MHz T^{-1} is the muon gyromagnetic ratio and ϕ = −29° is a phase shift.

This fitting function has three components: an oscillating component (A_1) coming from the static magnetism, a relaxing component (A_2) typical of measurements of polycrystalline magnetic materials, and a weakly relaxing component (A_3) which we ascribe to a non-magnetic background such as might come from muons landing in the cryostat after missing the sample or failing to stop within it. Fig. 6b shows the temperature dependence of the internal field. The internal field falls off rapidly with increasing temperature, and above 2.2 K no oscillations can be resolved in the μ^+SR data. This suggests that the magnetic transition occurs at $T_N \approx 2.1(1)$ K.

The spectra measured above the magnetic transition between $2.5 \le T \le 10$ K show little variation with temperature. An example spectrum measured at T = 10 K is shown in Fig. 6a and is well characterized by a combination of exponential relaxation and a non-relaxing background. This is typical of relaxation due to dynamic fluctuations of the electronic moments in a paramagnet. In materials of this type, positive muons would be expected to stop near electronegative fluorine atoms where they interact with the fluorine nuclei via a dipole–dipole interaction and give rise to a so-called F-μ spectrum, as seen in several related systems [43]. However, in **2** we do not resolve a clear F-μ spectrum. There is a slight change in the shape of the spectrum in Fig. 6a around 2 μs that might suggest a contribution from such a signal with a very low amplitude. This implies that the dynamic fluctuations of the electronic moments obscure any F-μ signal.

3.3. Structural and magnetic properties of $[Ni(gly)_2(pyz)]\cdot 5.21H_2O$ (**3**)

3.3.1. Crystal structure

The local structure about the Ni(II) center in **3** is composed of two *trans*-O-atoms, two *trans*-N-atoms from chelated gly ligands and two N-atoms belonging to pyz (Fig. 7a). Established by average d(Ni-N) and d(Ni-O) distances of 2.097(4) and 2.059(3) Å, respectively, we assign the four N-atoms to the equatorial plane and the two O-atoms to axial sites. Chelation of the gly ligands to the Ni(II) center yields strongly distorted bond angles surrounding it, with O1-Ni-N1 being 80.7(2)°. The non-planar configuration of gly is due to sp^3 hybridization of $C2$ and C4. This chelation may affect the coordination geometry of the pyz ligand which leads to a slightly non-linear N3-Ni-N4 bond angle of 177.2(2)°.

Akin to (**1**) and (**2**), the pyz ligands are bidentate and form bridges between neutral $[Ni(gly)_2]$ units to produce linear chains (Fig. 7a) that propagate along the b-axis. Along the chain, the Ni(II) ions are uniformly separated by 6.980(1) Å and the

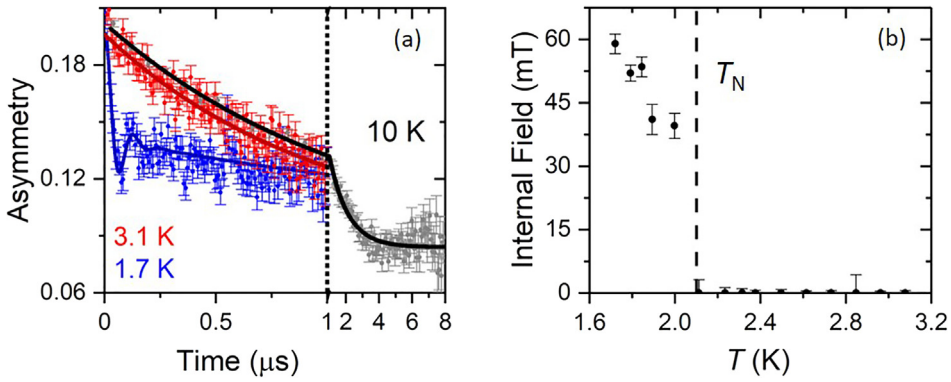

Fig. 6. (a) Measured μ^+SR spectra (●) for **2** obtained at 1.7, 3.1 and 10 K. Solid lines are fits to the data as described in the text. (b) T-dependence of the internal field B extracted by fitting the data in (a) to Eq. (2).

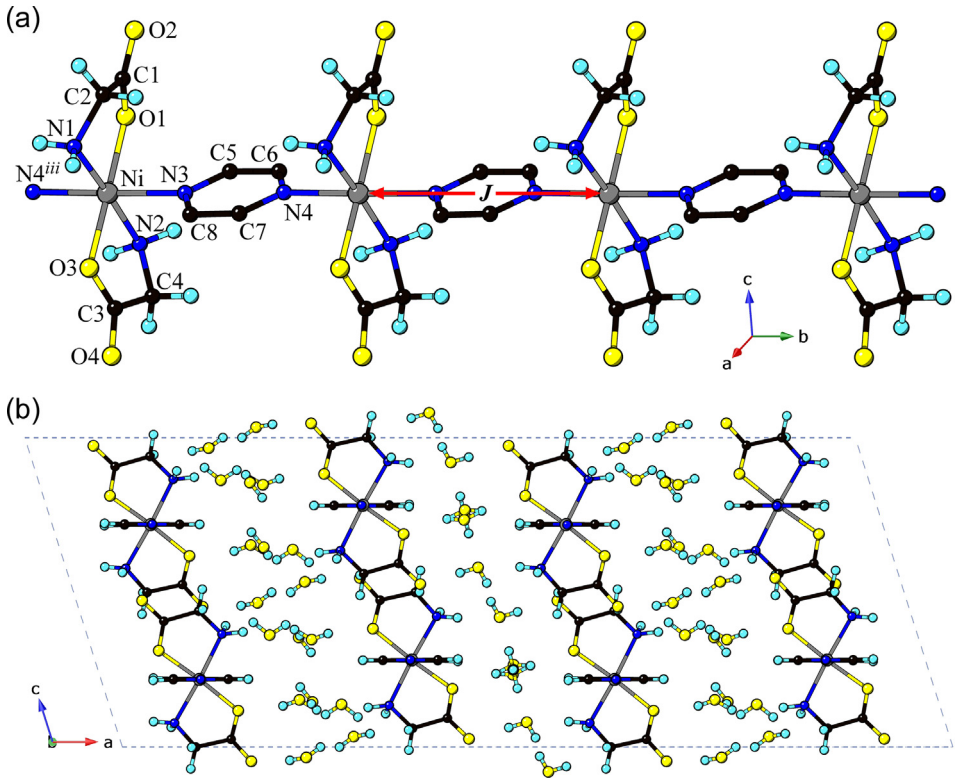

Fig. 7. (a) Segment of a linear chain for $[Ni(gly)_2(pyz)]\cdot 5.21H_2O$ (**3**). Pyrazine H-atoms and interstitial H_2Os are omitted for clarity. Symmetry code: (*iii*) (x, $y + 1$, z) (b) Quasi-2D packing of chains viewed down the *b*-axis. Note the variation in the number of lattice H_2Os filling between the sheets. The unit cell is indicated by gray dashes.

Ni-N3···N4 angle is 178.7(2)°. Neighboring chains stagger along the *b*-axis and pack to form planar sheets within the *bc*-plane as shown in Fig. 7b. The closest *d*(Ni···Ni) separation is 7.054(1) Å and only slightly longer than the intrachain distance. There are four such sheets per unit cell which stack along the *a*-axis. Channels between adjacent sheets are alternately filled by a variable number of H_2O molecules that are extensively connected through O···H bonds ranging in length from 1.85 to 2.65 Å.

3.3.2. Magnetic susceptibility

The $\chi(T)$ data rises as the temperature is lowered and exhibits a maximum at ≈ 2.5 K, in keeping with the presence of weak magnetic exchange. As plotted in the inset of Fig. 8a, a Curie-Weiss model was used to fit to $1/\chi(T)$ above 50 K to afford the parameters: $g = 2.23(1)$, $\theta_{CW} = -1.3(3)$ K and a temperature-independent term $\chi_0 = 1.2(2) \times 10^{-9}$ m^3 mol^{-1}. The small θ_{CW} value is consistent with the expectedly weak AFM exchange coupling along Ni-pyz-Ni.

3.3.3. Pulsed-field magnetization

Pulsed-field $M(H)$ data were calibrated using SQUID data and found to saturate at 2.3(1) μ_B, consistent with the *g*-factor obtained from the $\chi(T)$ data (Fig. 8a). The powder differential susceptibility (Fig. 8b) shows two critical fields; $\mu_0 H^x_{sat}$ at 1.8(2) T and saturation $\mu_0 H^z_{sat}$ at 12.5(5) T. Within the easy-plane model these fields imply $n\langle J\rangle = 1.4(2)$ K and $D = 8.0(6)$ K. The chelating gly ligand induces a low symmetry of the Ni(II) center which will likely yield a non-zero *E*-term, thus 8.0 K is an upper limit on *D*.

3.4. Structural and magnetic properties of $Ni(AF_6)(vinim)_4$ [A = Ti (**4**), Zr (**5**)]

3.4.1. Crystal structure

While $Ni(SiF_6)(vinim)_4$ was reported some years ago, its crystal structure was not determined but inferred from that of the structurally-characterized Co(II)-analog [44]. We synthesized the $[TiF_6]^{2-}$ (**4a** and **4b**) and $[ZrF_6]^{2-}$ (**5**) congeners and show via X-ray diffraction methods that they are structurally similar to $Co(SiF_6)(vinim)_4$. The structures were determined by Rietveld refinement of synchrotron powder diffraction (**4a**; Fig. 9) and laboratory-based single crystal X-ray diffraction data (**4b** and **5**).

The difference in crystalline properties are attributed to ordered (**4a** and **5**) and disordered (**4b**) vinim ligands. For ordered vinim molecules (Fig. 10a), even partially, a lower symmetry permits finite intensity for $h + k + l$ = odd Bragg reflections (* in Fig. 9; inset) and the relevant space group is $P4_2/n$. Alternatively, positional disorder (Fig. 10b) of the vinim ligands affords higher crystal symmetries and extinctions in the X-ray diffraction pattern conducive to space group $I4/m$. Fig. 9 compares the experimental data to the predicted pattern for each space group assignment. Crushing crystals of **4b** into a fine powder leads directly to **4a** (see Fig. S3).

The differing structural symmetries for both forms of $Ni(TiF_6)(vinim)_4$ reveal key differences with regard to the pseudo-octahedral NiN_4F_2 environment with F-atoms located on axial sites. For the case of $P4_2/n$ (**4a**), there are four equivalent Ni-N1 bond distances of 2.005(4) Å and two longer Ni-F1 distances of 2.076(3) Å. The bond angles making up the Ni coordination sphere are nearly ideal with the largest distortions being 88.4(3) and 176.7(3)°. In the $I4/m$ system (**4b**), the four-fold axis runs through the F-Ni-F axis which generates four equivalent Ni-N1 distances of 2.070(1) Å and two equivalent Ni-F1 bonds of 2.072(1) Å. Thus, the Ni coordination sphere may essentially be described as isotropic. All of the F1-Ni-F1, F1-Ni-N1 and N1-Ni-N1 bond angles are ideal at 90 and 180°.

In **5**, the Ni(II) and Zr(IV) centers have two-fold symmetry with-respect-to the *c*-axis. Atom F1 occupies the glide plane perpendicular to the *c*-direction. The Ni(II) center is isotropic with equal *d*(Ni-N1) and *d*(Ni-F1) bond distances of 2.078(1) Å whereas the *d*(Zr-F1) and *d*(Zr-F2) bond lengths are slightly different at 2.029

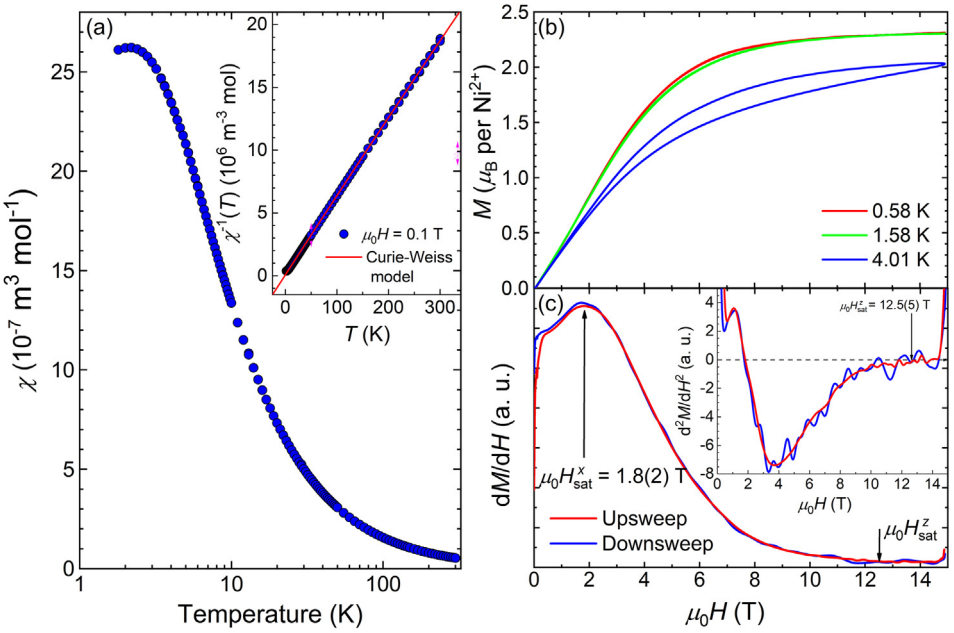

Fig. 8. Magnetometry data for powder samples of **3**. (a) $\chi(T)$ measured at μ_0H = 0.1 T. Inset shows $1/\chi(T)$ (●) and the fit to a Curie-Weiss model (red line) for $50 \leq T \leq 300$ K. (b) Pulsed-field magnetization calibrated using DC-field SQUID data. (c) Low temperature dM/dH upsweeps at T = 0.6 K with the indicated features corresponding to critical fields. The inset shows d^2M/dH^2 used to determine $\mu_0H^z_{sat}$. (For interpretation of the references to colour in this figure legend, the reader is referred to the web version of this article.)

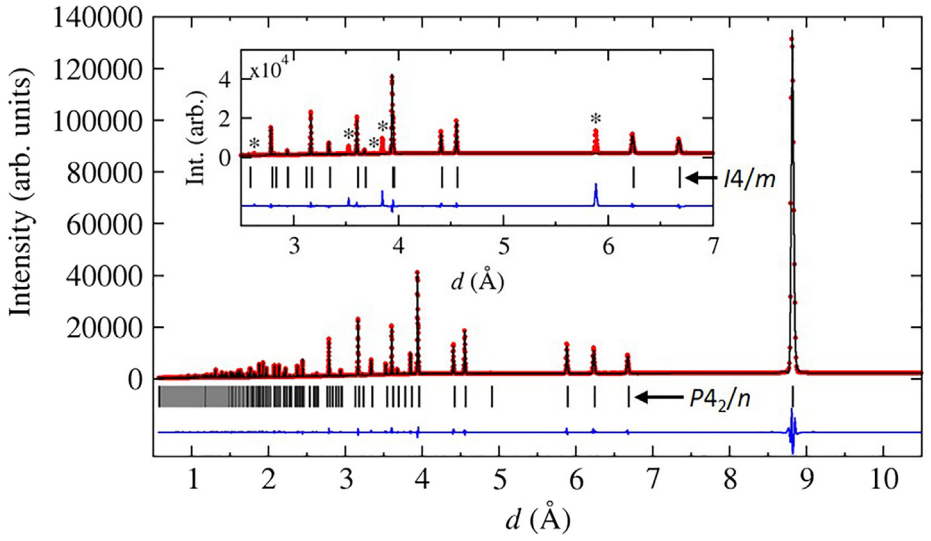

Fig. 9. T = 100 K X-ray powder diffraction data (●) for an as-precipitated sample of **4a** comparing Rietveld refinements (—) in space groups $P4_2/n$ (main) and $I4/m$ (inset). Asterisks in the inset plot mark additional peaks, (1 1 1), (2 2 1), (3 1 1), (2 1 2) and (4 2 1) expected for $P4_2/n$. Difference plots ($I_{obs} - I_{calc}$) are shown as blue lines at the bottom. (For interpretation of the references to colour in this figure legend, the reader is referred to the web version of this article.)

(1) and 1.995(1) Å, respectively. Bond angles around each metal center deviate from the ideal octahedral angles with the most distorted being 88.39(1)° for F1-Ni-N1 and 88.04(1)° for F1-Zr-F2. *Trans*-N-Ni-N bond angles are non-linear at 176.78(3)° while the equatorial F-Zr-F bond angle is 176.08(2)°. The ethylene portion of each vinim ligand occupies roughly the same plane as the imidazole ring to which it is attached.

The $[ZrF_6]^{2-}$ ion links $[Ni(vinim)_4]^{2+}$ units through F1-atoms to afford linear 1D chains with d(Ni···Zr) distances of 4.107(1) Å (Fig. 10a). A comparison among the $[AF_6]^{2-}$ derivatives yields d(Ni···Ni) separations that vary from 7.89890(2) Å (**4a**) to 8.1946 (7) Å (**5**), consistent with an increase in M(IV) ionic radius. Within a chain, one *trans*-pair of vinim ligands form bifurcated C-H···F hydrogen bonds, notably C1-H1···F2 [d(H1···F2) = 2.23(1) Å; C1-H1···F2 = 174.7(2)°] and C3-H3···F2 [d(H3···F2) = 2.56(1) Å; C3-H3···F2 = 171.7(2)°], with one $[ZrF_6]^{2-}$ unit as shown by orange dashes in Fig. 10a while the remaining *trans*-pair interacts with the other $[ZrF_6]^{2-}$ moiety.

Adjacent chains are staggered by 1/2c leading to large interchain d(Ni···Ni) distances of no less than 9.757(1) Å. Weak van der Waals interactions hold the chains together but do not provide effective exchange pathways. Thus, the chains may be described as being magnetically isolated.

3.4.2. Magnetic susceptibility

Powdered susceptibility data for both compounds shows a slow rise to a plateau-like feature that develops at temperatures below T < 10 K (Fig. 11a and b) and resembles the data expected for an

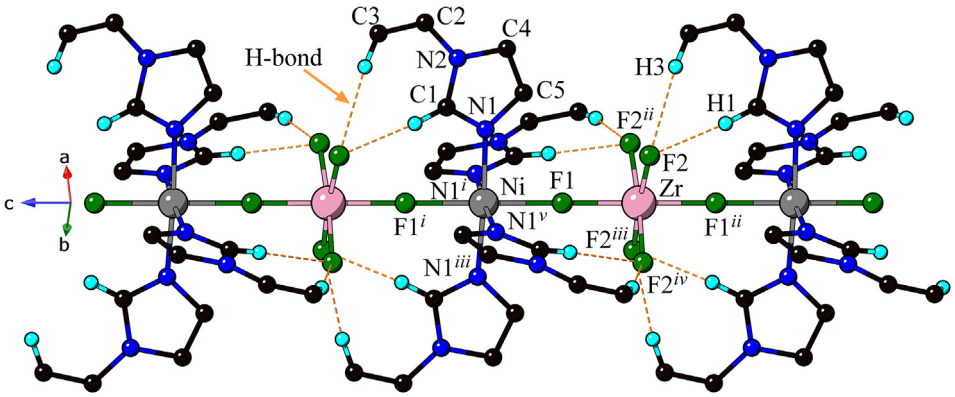

Fig. 10. (a) Segment of an infinite polymeric chain of $Ni(ZrF_6)(vinim)_4$ (**5**) with most H-atoms omitted for clarity. A single unit cell contains four such chains propagating parallel to the *c*-axis. Symmetry codes: (*i*) (*y*, −*x* + 3/2, −*z* − 1/2); (*ii*) (*y*, −*x* + 3/2, −*z* + 1/2); (*iii*) (−*x* + 3/2, −*y* + 3/2, *z*); (*iv*) (−*y* + 3/2, *x*, −*z* + 1/2); (*v*) (−*y* + 3/2, *x*, −*z* − 1/2). Hydrogen bonds F2···H1 and F2···H3 are indicated by orange dashes. The structure of **4a** (*A* = Ti), as obtained from powder diffraction methods, is identical. (b) Local structure of **4b** highlighting 50/50 disordered vinim ligands with H-atoms removed for clarity purposes. A disordered version of **5** was not observed. (For interpretation of the references to colour in this figure legend, the reader is referred to the web version of this article.)

ensemble of $S = 1$ moments with single-ion anisotropy, but no significant exchange interactions [10]. Both materials are fitted well by a *D*-only powder-average model [10,45] along with a small χ_0.

For compound **4a**, the fit is good and returns estimates of $D = 24.9(1)$ K, $g = 2.132(3)$ and $\chi_0 = 1.5(1) \times 10^{-8}$ m^3 mol^{-1}. This value of *D* is in reasonable agreement with the ESR data (see below), however, the *g*-value is a little smaller than expected for Ni(II) ions in this local environment and lower than the powder average ESR value of $g = 2.21$. Fitting the inverse suceptibility to a Curie-Weiss law, inset of Fig. 11a, yielded $g = 2.28(1)$, $\theta_{CW} = -3.6(2)$ and $\chi_0 = 3(1) \times 10^{-10}$ m^3 mol^{-1}.

For **5**, the *D*-only model fits the $\chi(T)$ data well over the entire *T*-range but with a slight departure at low temperatures. The parameters estimated from the fit are $D = 18.5(1)$ K, $g = 2.18(1)$ and $\chi_0 = 1.3(2) \times 10^{-9}$ m^3 mol^{-1}, in reasonable agreement with the ESR (see below). A fit of $1/\chi(T)$ between 50 and 300 K yielded a good agreement for the parameters $g = 2.19(1)$, $\theta_{CW} = 1.2(9)$ K and $\chi_0 = 5.1(9) \times 10^{-9}$ m^3 mol^{-1}.

3.4.3. Pulsed-field magnetization

In both compounds, we would expect to see a bump in d*M*/d*H* corresponding to the field at which the $m_z = 1$ energy level crosses the $m_z = 0$ ground state energy level for fields applied along the magnetic hard-axis, as described in [10,46]. However no clear features are observed in the data (inset to Fig. 11c). It is possible that a significant amount of the polycrystalline sample reorients during a pulsed-field measurement, aligning the easy-plane with the applied field. This would reduce the size of the feature observed at the level crossing for subsequent pulses.

3.4.4. Electron-spin resonance

The Ti-complex **4a** exhibits high-field ESR spectra of poor quality however, estimates of g_z and *D*-values [2.2(2) and 23.8(5) K, respectively], can be made. Similar (although better quality) spectra were obtained for **5**, from which $g_z = 2.22(1)$ and $D = 20.0(5)$ K were determined. Electronic structure calculations give $D = 18.1$

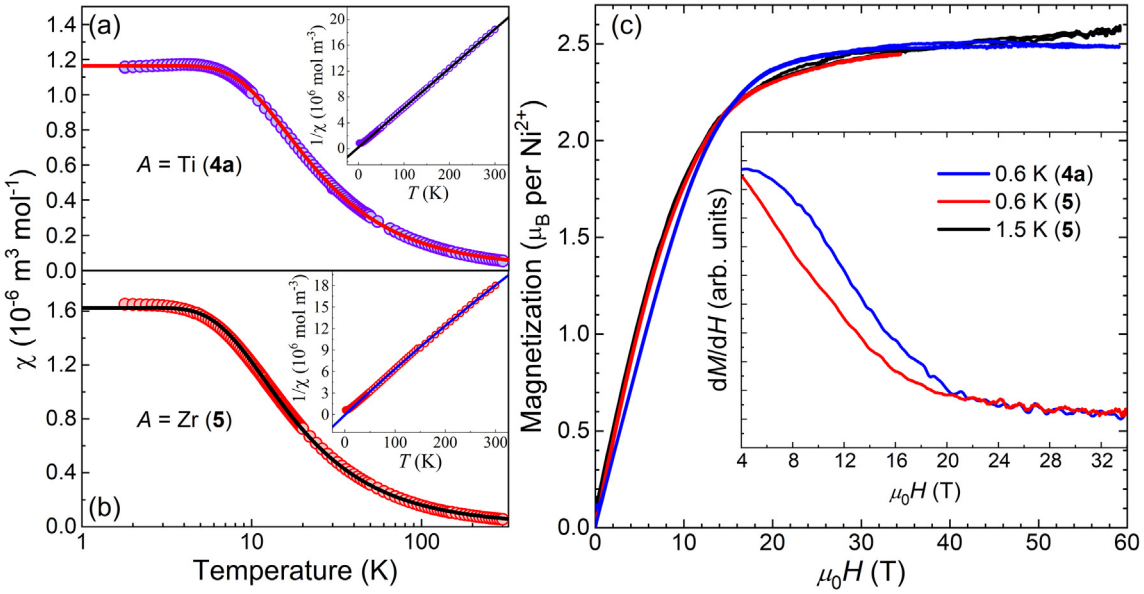

Fig. 11. Magnetometry data for powder samples of **4a** and **5**. (a) $\chi(T)$ for **4a** (○) fit to a *D*-only powder average model (red line) measured at $\mu_0 H = 0.1$ T. Inset shows $1/\chi(T)$ (○) fit to a Curie-Weiss model (black line) (b) $\chi(T)$ for **5** (○) measured at $\mu_0 H = 0.1$ T with a *D*-only powder average model fit (black line) with the inset showing $1/\chi(T)$ (○) fit with a Curie-Weiss law (blue line). (c) Pulsed-field $M(H)$ for both compounds calibrated using SQUID data. The powder-averaged saturation moment predicted by ESR for **4a** (blue dashes) is plotted for comparison. The inset shows d*M*/d*H* for both compounds. (For interpretation of the references to colour in this figure legend, the reader is referred to the web version of this article.)

and 16.9 K for **4a** and **5**, respectively, which are in keeping with the experimental trend.

3.5. Structural and magnetic properties of $[Ni(SiF_6)(mepz)_4(H_2O)]\cdot H_2O$ (**6**)

3.5.1. Crystal structure

Reaction between $NiSiF_6$ and four equivalents of 4-methylpyrazole leads to deep blue crystals of **6**. The material crystallizes in the monoclinic space group *Cc* with $Z = 4$. From Fig. 12 it can be seen that neutral molecules of $Ni(SiF_6)(mepz)_4(H_2O)$ feature axial sites occupied by $[SiF_6]^{2-}$ [*d*(Ni-F1) = 2.130(2) Å] and H_2O ligands [*d*(Ni-O1) = 2.063(2) Å]. Equatorial Ni-N distances range from 2.065(3) to 2.105(3) Å. Bond angles around the Ni(II) center deviate appreciably from the ideal octahedral angles with N5-Ni-O1 and N5-Ni-N1 being the most distorted at 94.4(1)° and 174.6(1)°, respectively. The distortive behavior arises from intramolecular hydrogen bond formation between pyrazole N-H moieties and equatorial F-atoms of the $[SiF_6]^{2-}$ anion. Orange dashed lines in Fig. 12 represent these interactions which have distances of 1.88(5)-2.08(5) Å and N-H···F bond angles of roughly 167(4)–173(4)°.

Owing to intermolecular O1-H1B···F4 hydrogen bond interactions, the molecules pack to form pseudo-1D chains [*d*(H1B-F6) = 1.92(5) Å; bond angle = 165(4)°]. Atom H1A interacts with the lattice H_2O (not shown in Fig. 12). Van der Waals interactions hold the chains together leading to negligible magnetic couplings.

3.5.2. Magnetic susceptibility

The powder DC susceptibility of **6** (Fig. 13a) rises as the temperature is lowered until a plateau is reached below $T = 3$ K. The data are suggestive of a system with little or no exchange coupling and easy-plane anisotropy [10]. We use a model containing both *D* and *E* anisotropy terms to fit the $\chi(T)$ data, yielding good agreement for the parameters: $D = 11.25(2)$ K, $E = 0.6(1)$ K and $g = 2.25(1)$. These are within the errors of the parameters obtained from the $M(H)$ measurements below. As compared to NiN_4F_2 in **5**, we notice that replacing one axial F-ligand with H_2O in **6** leads to a nearly 50% reduction in the *D*-value.

3.5.3. Pulsed-field magnetization

Pulsed-field measurements for a powder sample rises slowly to saturation (Fig. 13b) in keeping with a large *D*. The data were calibrated using the SQUID results and show that **6** saturates at 2.25(1) μ_B; this suggests $g = 2.25(1)$, in excellent agreement with the value of *g* obtained from the $\chi(T)$ data. The differential magnetization at 0.58 K drops smoothly until a bump emerges at ≈ 8 T. This is characteristic of an easy-plane Ni(II) compound that exhibits negligible magnetic interactions [10]. The data continue to decline beyond the bump. The position of $\mu_0 H_c$ was found from the midpoint of the peak derivative shape in the d^2M/dH^2 data and was located at $\mu_0 H_c = 7.8(6)$ T; using the results from [10], an estimate of $\sqrt{D^2 - E^2} = 11.8(7)$ K was obtained which agrees very well with the fit of $\chi(T)$.

3.5.4. Electron-spin resonance

Low-temperature ESR spectra recorded for powdered **6** were obtained over the frequency range $100 \leq \nu \leq 326.4$ GHz (Fig. 13a). The 108, 208 and 326.4 GHz spectra were measured at 5 K while all other spectra were obtained at the base temperature of the cryostat (≈ 3 K). Resonances corresponding to high-field *x* (γ_x) and *y* (γ_y) transitions were observed in the 104 and 108 GHz sweeps. The high-field *z* (γ_z) transition is the most intense resonance for $\nu \leq 208$ GHz and gives a direct measure of *D* by linearly extrapolating the position of the transition at different ν back to zero. The zero-field intercept occurs at ≈ 230 GHz, which corresponds to a zero-field splitting energy of ≈ 11 K. The 108 GHz and 208 GHz sweeps were also measured at 30 K. Fig. 14 shows that the *X* and *Y* features, seen in the 30 K, 208 GHz spectrum at 9.2 T and 10.2 T, respectively, become frozen out when *T* is lowered to 5 K. This is indicative of easy-plane anisotropy in **6**. The γ_y transition is only observed in the high-temperature data (Inset of Fig. 14b), providing further evidence that $D > 0$. The half-field *z* (α_z) transition also figures prominently in the low-frequency sweeps. For $\nu \geq 230$ GHz, the low-field *x* (β_x), *y* (β_y) and *z* (β_y) transitions are observed. Apparent features that likely correspond to the half-field *x* (α_x) and *y* (α_y) transitions are positioned to the high-field side of β_z in the 326 GHz spectra, though spectral noise makes it difficult to accurately resolve their positions.

The observed transitions were plotted and fitted to a *D*- and *E*-only model (Fig. 15). The parameters $D = 11.45(2)$ K, $E = 0.49(1)$ K, $g_x = 2.240(7)$, $g_y = 2.228(5)$ and $g_z = 2.158(5)$ were extracted, and the model is in good agreement with the data. A 326 GHz simulation using these parameters at 5 K is shown in Fig. 15 and recreates the β_x and β_y transitions. The simulated β_z resonance at 3 T is also in good agreement with the data, whilst the α_x and α_y resonances are shown to lie in the noisy region to the high-field side of β_z, confirming the above interpretation. The fact that $g_x > g_z$ is consistent with easy-plane anisotropy and a value of $\lambda = -279$ K is obtained for the spin–orbit coupling parameter. This is of the same order of magnitude as that anticipated for Ni(II) ions [8]. Thus, the parameters obtained from the magnetometry and ESR measurements are in very good agreement.

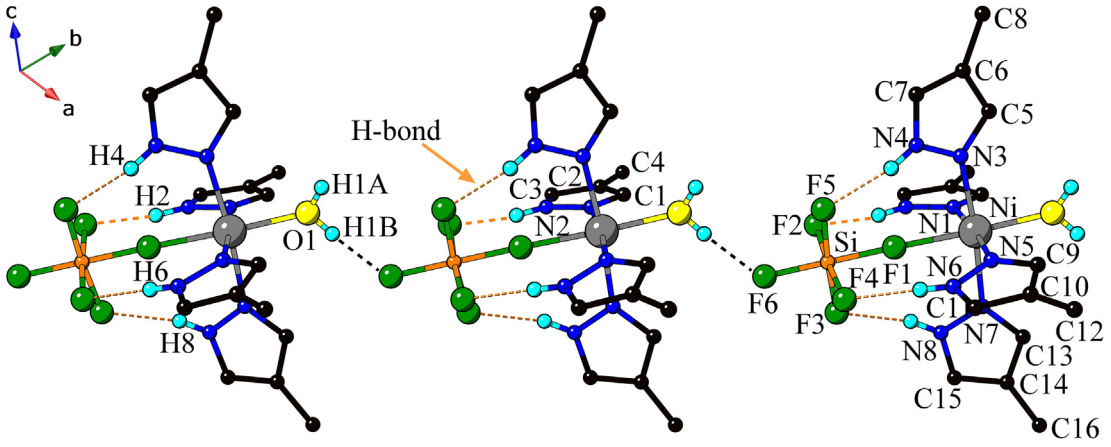

Fig. 12. Crystal structure and atom labeling scheme for $[Ni(SiF_6)(mepz)_4(H_2O)]\cdot H_2O$ (**6**). Lattice H_2O and most mepz H-atoms have been omitted for clarity. Intra- and intermolecular H-bonds are delineated by orange and black dashes, respectively. (For interpretation of the references to colour in this figure legend, the reader is referred to the web version of this article.)

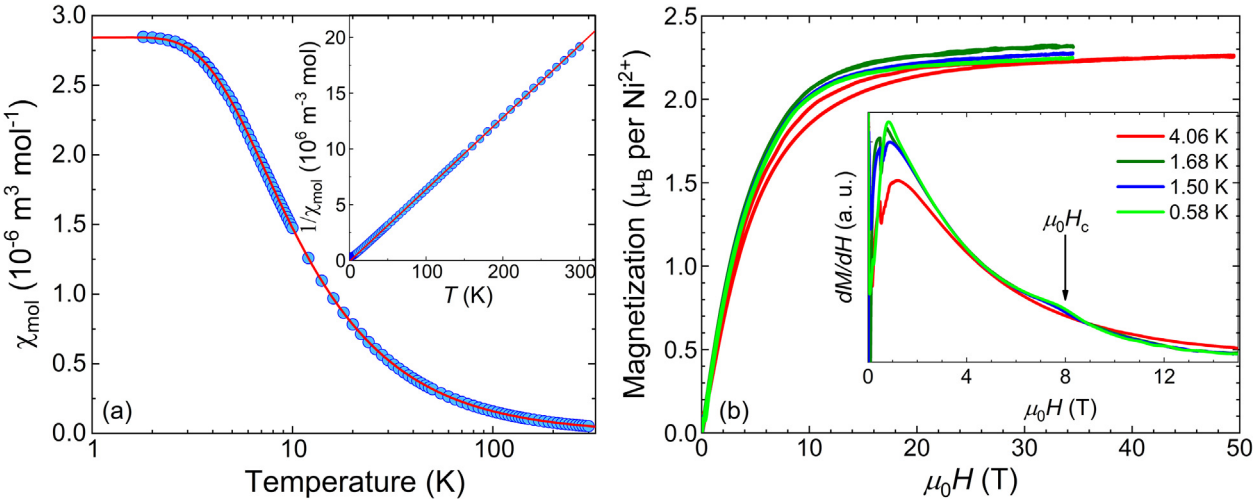

Fig. 13. (a) Magnetic susceptibility data (●) and *D*-only model fit (red line) for **6**. The inset shows $1/\chi(T)$ and the corresponding fit to a Curie-Weiss law (red line). Fit parameters for both plots are given in the text. (b) Pulsed-field $M(H)$ data taken at several temperatures (main plot) and dM/dH (inset). The critical field ($\mu_0 H_c$) is indicated in the inset and corresponds to the T = 0.58 K data. (For interpretation of the references to colour in this figure legend, the reader is referred to the web version of this article.)

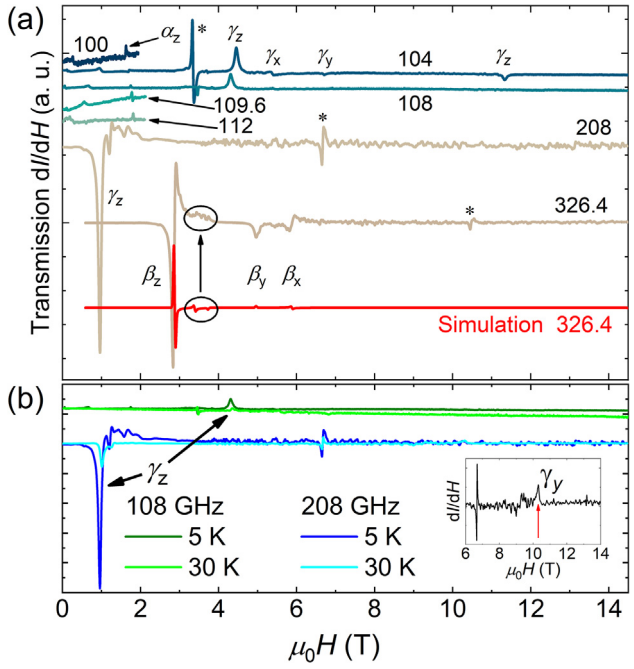

Fig. 14. (a) ESR spectra of powdered **6** labelled in GHz for each spectra. Measurements were performed at ≈ 3 K (100, 104, 109.6, and 112 GHz) and 5 K (108, 208 and 326.4 GHz). Resonances of known transitions are labelled. The resonances marked with * are unidentified. A 5 K simulation at 326.4 GHz with the parameters obtained from a *D* and *E* only fit to the observed resonances has been added in good agreement with the data. The circled resonances in the 326 GHz data and simulation correspond to the α_x and α_y transitions. (b) Temperature dependent ESR spectra at 108 and 208 GHZ. The decrease in the intensity of the γ_z transition as the temperature is increased is clearly observed in both spectra, indicating $D > 0$. Inset: 30 K ESR spectra at 208 GHz showing the γ_y transition at 10.3 T. This is not observed in the low T data and further substantiates $D > 0$.

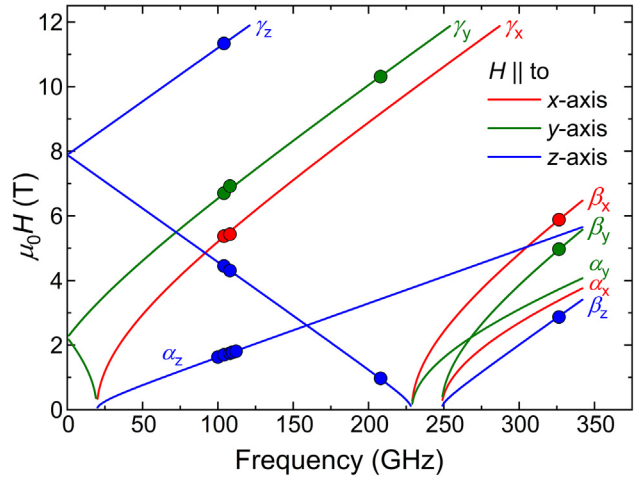

Fig. 15. Magnetic field vs. frequency plot for **6**. Fitting of the transitions from Fig. 14 to a *D*- and *E*-only model which yields the parameters g_x = 2.240(7), g_y = 2.228(5), g_z = 2.158(5), D = 11.45(2) K and E = 0.49(1) K, in good agreement with the data and results from the magnetometry study.

3.6. Structural and magnetic properties of $NiF_2(OHpy)_4$ (**7**)

3.6.1. Crystal structure

Akin to the previously reported chloride complex [47], the fluoride compound also crystallizes in the orthorhombic space group *Pccn* with four discrete molecules per unit cell (Fig. 16a). Each NiN_4F_2 octahedron is slightly compressed with the Ni(II) ion possessing two-fold rotational symmetry along the F1-Ni-F1^i axis. Four OHpy molecules coordinate to the Ni equatorial sites with an average *d* (Ni-N) bond distance of 2.107(2) Å. The two axial Ni-F bonds are equal at 2.055(2) Å. The distortion exhibited by the NiN_4F_2 octahedron is noted by the F1-Ni-N1 and F1-Ni-F1^i bond angles of 86.16(7) and 177.11(8)°, respectively, which deviate appreciably from the ideal 90 and 180° angles. Bond distances and angles within the pyOH ligand are typical of this molecule. Of note is the coplanarity of the hydroxyl substituent relative to the pyridine ring.

Within the unit cell (Fig. 16b), it can be seen that the $NiF_2(OHpy)_4$ molecules pack in two unique orientations relative to one another. This allows intermolecular O-H···F hydrogen bonds to link molecules into a quasi-2D lattice, with the shortest intralayer *d*(Ni···Ni) separations being 7.377 and 9.179 Å. Each F1-atom forms bifurcated H-bonds with H1 and H2 at distances of 1.775 and 1.725 Å, respectively, and nominal bond angles O1-H1···F1 = 161.4° and O2-H2···F1 = 169.1°.

3.6.2. Magnetic susceptibility

SQUID magnetometry data in the form of $\chi(T)$ are shown in Fig. 17a and are typical of a system of non-interacting anisotropic

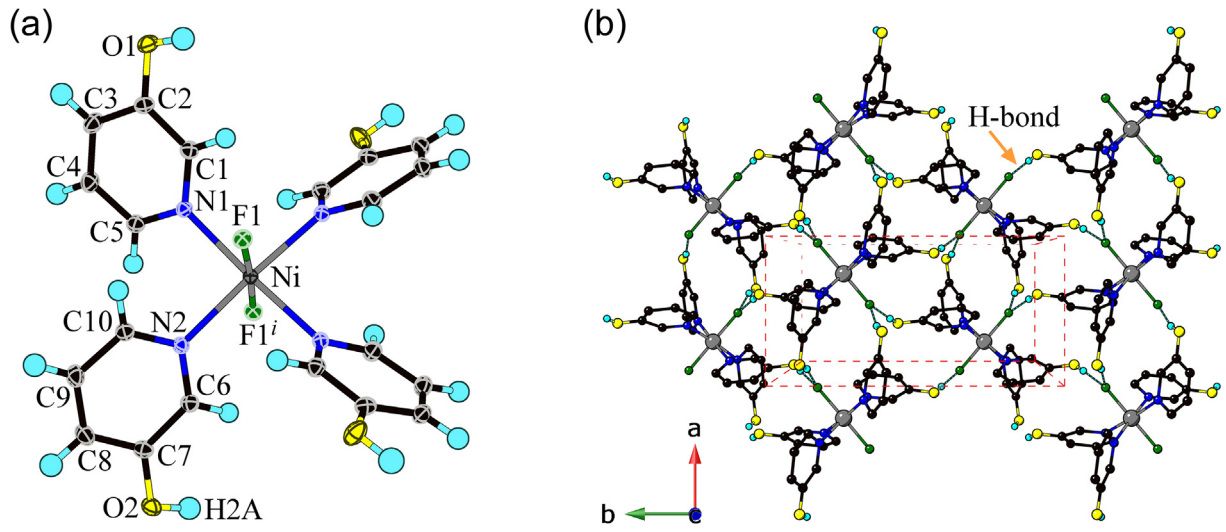

Fig. 16. (a) Molecular structure and atom labeling scheme for $NiF_2(OHpy)_4$ (**7**) determined at 100 K. Thermal ellipsoids are drawn at the 40% probability level. Symmetry code: (*i*) (−*x* + 1/2, −*y* + 1/2, *z*). (b) Quasi-2D molecular packing in **7**; H-bonds are delineated by dashed black lines. The unit cell is shown as red dashes and pyridyl H-atoms are omitted for clarity. (For interpretation of the references to colour in this figure legend, the reader is referred to the web version of this article.)

S = 1 moments. The $\chi(T)$ data were modelled over the $1.8 \leq T \leq 300$ K range using a conventional powder-average model describing the magnetocrystalline anisotropy for an *S* = 1 ion; $J = J' = 0$ is assumed in Eq. (1) [10,46]. Intermolecular H-bond mediated exchange is likely to be very weak in this material. From a least-squares fit (solid line in Fig. 17a), we obtain g = 2.16, D = 12.3(5) K, E = 1.9(1) K and $\chi_0 = 4.3 \times 10^{-9}$ m^3 mol^{-1} (fixed).

3.6.3. Magnetization

Pulsed-field $M(H)$ vs $\mu_0 H$ data were measured at several temperatures between 0.5 and 10 K and at fields up to 30 T; data are shown in Fig. 17b. At the highest fields measured, M saturates close to 2.1–2.2 μ_B as expected from the g-value obtained from the $\chi(T)$ data. The absence of a spin-flop transition is consistent with $D > 0$ [11]. Applying the easy-plane model to the weak bump seen in dM/dH [11], we estimate $\sqrt{D^2 - E^2}$ = 12.2(3) K which is in very good agreement with the $\chi(T)$ result.

3.6.4. Electron-spin resonance

Spectra measured at 10 K reveal signals indicative of isolated Ni(II) complexes (blue line in Fig. 18a). Simulating these data, of which examples taken at 305.1 and 630.9 GHz are shown as the red line in Fig. 18a, we find g_x = 2.205(5), g_y = 2.220(3), g_z = 2.151(5), D = 12.36(1) K and E = 1.16(1) K. The anisotropy values are in good agreement with those obtained from magnetometry measurements. The field-frequency profile is shown in Fig. 18b where it can be seen that the observed values occur at the expected resonances determined by the g, D and E-parameters.

4. Conclusions

For the *S* = 1 Ni(II) coordination complexes studied here, including molecules and polymers, we showed that $D > 0$ can be forecast with good accuracy for six-coordinate *trans*-ligated NiN_4F_2, NiN_4O_2 and NiN_4OF systems. The Ni-N bond lengths are equal to or slightly longer than axial Ni-*L* giving isotropic or slightly compressed octahedra, respectively. A qualitative model based on the d(Ni-L_{ax})/d(Ni-N_{eq}) ratio shows an overall good correlation with the magnitude of D (Fig. 19) and, from the spectrochemical series, the anticipated ligand-field strength is: $F \approx HF_2^- \ll H_2O \ll$ gly < amines.

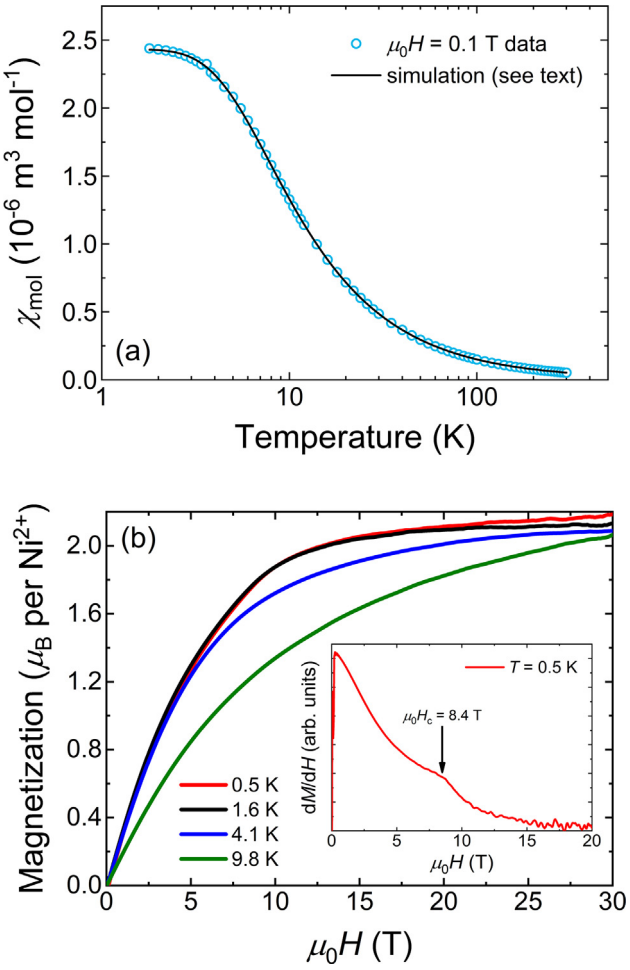

Fig. 17. (a) $\chi(T)$ vs. T on a logarithmic and (b) low-T pulsed-field M data obtained for powder samples of **7**. The inset of (b) shows the T = 0.5 K dM/dH plot highlighting the bump at 8.4 T as described in the text.

Reduced D-values occur for increasingly covalent Ni-*L* bonds and D is largest in cases when the Pauling electronegativity (EN) of axial and equatorial donor atoms differ the most. As the separation in

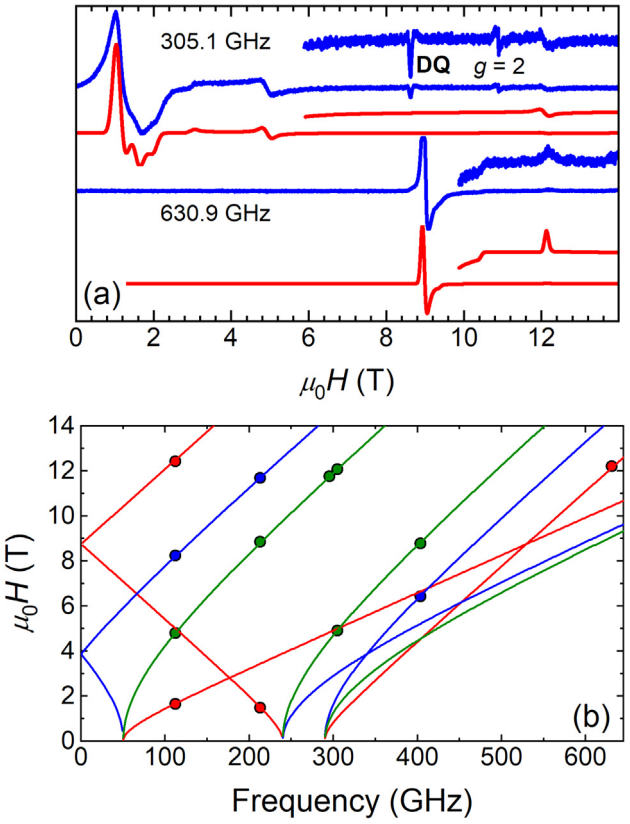

Fig. 18. T = 10 K ESR data for **7**. (a) Measured (blue line) and simulated (red line) spectra at f = 305.1 and 630.9 GHz. (b) field-frequency profile with experimental data and calculated resonances shown as points and colored lines, respectively. (For interpretation of the references to colour in this figure legend, the reader is referred to the web version of this article.)

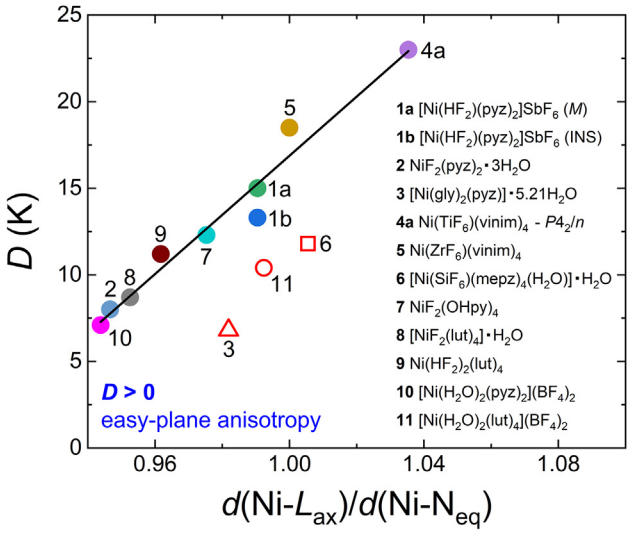

Fig. 19. Magnetostructural D-correlation for compounds **1**–**7**. Data for **8**–**11** are from Refs. [10,48]. Compounds **3**, **10** and **11** consist of NiN_4O_2 coordination spheres while that of **6** is NiN_4OF.

donor-atom strength grows, D becomes increasingly more positive and we observe the largest values for NiN_4F_2; e.g., $Ni(TiF_6)(vinim)_4$ (**4a**), D = 25 K. Two other NiN_4F_2 compounds included in Fig. 19 are $[NiF_2(lut)_4]\cdot H_2O$ (**8**) and $Ni(HF_2)_2(lut)_4$ (**9**) (lut = 3,5-lutidine) which are described in detail elsewhere [48]. However, their smaller D-values are attributed to a larger difference in Ni-N and Ni-F bond lengths. For $[Ni(SiF_6)(mepz)_4(H_2O)]\cdot H_2O$ (**6**), replacing one F-donor with H_2O leads to a lower site symmetry about the Ni(II) ion and reduces D by nearly 50%. $[Ni(gly)_2(pyz)]\cdot 5.21H_2O$ (**3**) exhibits the smallest D of the materials studied which may be due, in part, to the close proximity of gly and pyz in the spectrochemical series.

The most striking observation in Fig. 19 is that d(Ni-L_{ax})/d(Ni-N_{eq}) deviates by only $\approx \pm 0.05$ compared to the isotropic case (=1.00) and yet, significant variation in D was found. This further highlights the extreme sensitivity of D to the ligand-field surrounding the Ni(II) ion. The fact that $[Ni(gly)_2(pyz)]\cdot 5.21H_2O$ (**3**), $[Ni(SiF_6)(mepz)_4(H_2O)]\cdot H_2O$ (**6**) and $[Ni(H_2O)_2(lut)_4](BF_4)_2$ (**11**) do not fit the correlation shown in Fig. 19 (solid line) suggests that other electronic factors such as the donor-atom electronegativity, π-character of Ni-N and Ni-L bonds, orbital reduction factors, etc., may be important and we are pursuing this further. Collectively, this work demonstrates an efficient and predictive model of easy-plane anisotropy in bespoke S = 1 Ni(II) quantum magnets.

CRediT authorship contribution statement

Jamie L. Manson: Conceptualization, Methodology, Visualization, Writing - original draft, review & editing, Supervision, Project administration, Funding acquisition. **Zachary E. Manson:** Resources, Investigation, Validation. **Ashley Sargent:** Resources, Investigation, Validation. **Danielle Y. Villa:** Resources, Investigation, Validation. **Nicole L. Etten:** Resources, Investigation, Validation. **William J.A. Blackmore:** Investigation, Formal analysis, Visualization, Writing - original draft. **Samuel P.M. Curley:** Investigation, Formal analysis, Visualization, Writing - original draft. **Robert C. Williams:** Investigation, Formal analysis, Visualization, Writing - original draft. **Jamie Brambleby:** Investigation, Formal analysis, Visualization. **Paul A. Goddard:** Methodology, Visualization, Writing - review & editing, Supervision, Data curation, Funding acquisition. **Andrew Ozarowski:** Investigation, Formal analysis, Visualization. **Murray N. Wilson:** Investigation, Formal analysis, Visualization, Writing - review & editing, Data curation, Funding acquisition. **Benjamin M. Huddart:** Investigation, Formal analysis, Visualization, Writing - review & editing, Data curation, Funding acquisition. **Tom Lancaster:** Investigation, Formal analysis, Visualization, Writing - review & editing, Data curation, Funding acquisition. **Roger D. Johnson:** Methodology, Investigation, Formal analysis, Software, Validation. **Stephen J. Blundell:** Investigation, Formal analysis, Visualization, Writing - review & editing, Data curation, Funding acquisition. **Jesper Bendix:** Methodology, Software, Validation. **Kraig A. Wheeler:** Formal analysis, Software, Validation, Funding acquisition. **Saul H. Lapidus:** Investigation, Formal analysis. **Fan Xiao:** Investigation, Formal analysis. **Serena Birnbaum:** Investigation, Formal analysis. **John Singleton:** Investigation, Formal analysis, Methodology, Visualization, Writing - review & editing, Supervision, Data curation, Funding acquisition.

Declaration of Competing Interest

The authors declare that they have no known competing financial interests or personal relationships that could have appeared to influence the work reported in this paper.

Acknowledgments

Work at EWU was supported by the U.S. National Science Foundation (NSF) under grant no. DMR-1703003. J.L.M. and K.A.W. gratefully acknowledge the NSF (CHE-1827313) for purchase of the single-crystal X-ray diffractometer at Whitworth University. This project has received funding from the European Research Council (ERC) under the European Union's Horizon 2020 research

and innovation program (grant agreement No. 681260). Use of the APS, an Office of Science User Facility operated for the U.S. Department of Energy (DOE) Office of Science by Argonne National Laboratory, was supported by the U.S. DOE under Contract No. DE-AC02-06CH11357. A portion of this work was performed at the National High Magnetic Field Laboratory, which is supported by NSF Cooperative Agreement No. DMR-1644779 and the State of Florida, as well as the Strongly Correlated Magnets thrust of the DoE BES "Science in 100T" program. The μ^+SR studies were carried out at the Swiss Muon Source, Paul Scherrer Institute, Switzerland and we are grateful for the provision of beamtime and to H. Luetkens for experimental assistance. This work was supported by EPSRC (UK) under grants EP/N023803/1, EP/N024028/1 and EP/N032128/1. The I11 beamtime was obtained through the Diamond Light Source Block Allocation Group award "Oxford/Warwick Solid State Chemistry BAG to probe composition-structure-property relationships in solids" (EE18786-15) and we thank L. Jia and G. Clarke for their assistance with measuring the data. B.M.H. acknowledges the STFC (UK) for the provision of a studentship. Data presented in this paper resulting from the UK effort will be made available at https://wrap.warwick.ac.uk/130808.

Appendix A. Supplementary data

CCDC 1956424−1956430 & 1956865 contains the supplementary crystallographic data for this paper. These data can be obtained free of charge via http://www.ccdc.cam.ac.uk/conts/retrieving.html, or from The Cambridge Crystallographic Data Centre, 12 Union Road, Cambridge CB2 1EZ, UK; fax: (+44) 1223-336-033; or e-mail: deposit@ccdc.cam.ac.uk.

Supplementary data to this article can be found online at https://doi.org/10.1016/j.poly.2020.114379.

References

[1] A.N. Vasiliev, O.S. Volkova, E.A. Zvereva, M.M. Markina, Low-Dimensional Magnetism, 1st ed., CRC Press, Boca Raton, 2019.
[2] For a recent review, see: A. Orendáčová, R. Tarasenko, V. Tkáč, E. Čižmár, M. Orendáč, A. Feher Cryst. 9 (6) (2019) 1–27.
[3] C.P. Landee, M.M. Turnbull, Eur. J. Inorg. Chem. (2013) 2266–2285.
[4] J.S. Miller, M. Drillon, Magnetism: Molecules to Materials I: Models and Experiments, 1st ed., Wiley-VCH, Weinheim, 2002.
[5] For a classic paper on low-dimensional magnetism, see: L.J. deJongh, A.R. Miedema Adv. Phys. 50 (2001) 947–1170.
[6] J.M. Kosterlitz, D.J. Thouless, J. Phys. C.: Sol. St. Phys. 6 (1973) 1181–1203.
[7] (a) F.D.M. Haldane, Phys. Rev. Lett. 50 (1983) 1153–1156;
(b) F.D.M. Haldane, Phys. Lett. A 93 (1983) 464–468.
[8] R. Boča, Coord. Chem. Rev. 248 (2004) 757–815.
[9] R.L. Carlin, Magnetochemistry, Springer-Verlag, Berlin, 1986.
[10] W.J.A. Blackmore, J. Brambleby, T. Lancaster, S.J. Clark, R.D. Johnson, J. Singleton, A. Ozarowski, J.A. Schlueter, Y.-S. Chen, A.M. Arif, S. Lapidus, F. Xiao, R.C. Williams, S.J. Blundell, M.J. Pearce, M.R. Less, P. Manuel, D.Y. Villa, J.A. Villa, J.L. Manson, P.A. Goddard, New J. Phys. 21 (2019) 093025.
[11] (a) J. Krzystek, A. Ozarowski, J. Telser, Coord. Chem. Rev. 250 (2006) 2308–2324;
(b) J. Telser, A. Ozarowski, J. Krzystek, Electron Paramag. Reson. 23 (2013) 209–263.
[12] A.F. Albuquerque, C.J. Hamer, J. Oitmaa, Phys. Rev. B 79 (2009) 054412.
[13] K. Wierschem, P. Sengupta, Mod. Phys. Lett. B 28 (2014) 1430017.
[14] (a) e.g. M. Orendáč, S. Zvyagin, A. Orendáčová, M. Sieling, B. Lüthi, A. Feher, M. W. Meisel Phys. Rev. B 60 (1999) 4170–4175;
(b) M. Orendáč, A. Orendáčová, J. Černák, A. Feher, P.J.C. Signore, M.W. Meisel, S. Merah, M. Verdaguer, Phys. Rev. B 52 (1995) 3435–3440.
[15] M. Orendáč, E. Čižmár, A. Orendáčová, J. Černák, A. Feher, M.W. Meisel, K.A. Abboud, S. Zvyagin, M. Sieling, T. Rieth, B. Lüthi, Phys. Rev. B 61 (2000) 3223–3226.
[16] J.L. Manson, S. Lapidus, P.W. Stephens, P.K. Peterson, H.I. Southerland, T. Lancaster, S.J. Blundell, A.J. Steele, J. Singleton, R.D. McDonald, Y. Kohama, R.E. Del Sesto, N.A. Smith, J. Bendix, S.A. Zvyagin, V. Zapf, P.A. Goddard, J. Kang, C. Lee, M.-H. Whangbo, Inorg. Chem. 50 (2011) 5990–6009.
[17] E.E. Castellano, O.R. Nascimento, R. Calvo, Acta Cryst. B38 (1982) 1303–1305.
[18] G.M. Sheldrick, SADABS and TWINABS, University of Göttingen, Göttingen, Germany, 2010.
[19] G.M. Sheldrick, Acta Crystallogr. A 71 (2015) 3–8.
[20] L.J. Barbour, J. Supramol. Chem. 1 (2001) 189–191.
[21] G.M. Sheldrick, Acta Crystallogr. C 71 (2015) 3–8.
[22] S.P. Thompson, J.E. Parker, J. Potter, T.P. Hill, A. Birt, T.M. Cobb, F. Yuan, C.C. Tang, Rev. Sci. Instr. 80 (2009) 075107.
[23] J. Wang, B.H. Toby, P.L. Lee, L. Rybaud, S.M. Antao, C. Kurtz, M. Ramanathan, R. B. Von Dreele, M.A. Beno, Rev. Sci. Instr. 79 (2008) 085105.
[24] J. Rodriguez-Carvajal, Physica B 192 (1993) 55–69.
[25] P.A. Goddard, J. Singleton, P. Sengupta, R.D. McDonald, T. Lancaster, S.J. Blundell, F.L. Pratt, S. Cox, N. Harrison, J.L. Manson, H.I. Southerland, J.A. Schlueter, New J. Phys. 10 (2008) 083025.
[26] S.J. Blundell, Contemp. Phys. 40 (1999) 175–192.
[27] L. Noodleman, J. Chem. Phys. 74 (1981) 5737–5743.
[28] F. Neese, ORCA Version 4.1.1, revision 2131 (2010) Max Planck Institute fuer Kohlenforschung, Muelheim/Ruhr, Germany.
[29] (a) F. Neese, Coord. Chem. Rev. 253 (2009) 526–563;
(b) S. Sinnecker, F. Neese, W. Lubitz, J. Biol. Inorg. Chem. 10 (2005) 231–238.
[30] (a) Yamaguchi, K.; Takahara, Y.; Fueno, T. In Applied Quantum Chemistry; Smith, V. H., Schafer, F., III, Morokuma, K., Eds.; D. Reidel: Boston, MA, 1986; p 155.;
(b) T. Soda, Y. Kitagawa, T. Onishi, Y. Takano, Y. Shigeta, H. Nagao, Y. Yoshioka, K. Yamaguchi, Chem. Phys. Lett. 319 (2000) 223–230.
[31] G.L. Stoychev, A.A. Auer, F. Neese, J. Chem. Theory Comput. 13 (2017) 554.
[32] F. Weigend, R. Ahlrichs, Phys. Chem. Chem. Phys. 7 (2005) 3297–3305.
[33] J. Brambleby, J.L. Manson, M.B. Stone, R. Johnson, P. Manuel, P.A. Goddard, J.A. Villa, C.M. Brown, J. Singleton, V. Zapf, S.H. Lapidus, R. Scatena, P. Macchi, Y.-S. Chen, L.-C. Wu, Phys. Rev. B 95 (2017) 134435.
[34] J. Liu, P.A. Goddard, J. Brambleby, F. Foronda, J. Möller, A. Ardavan, S.J. Blundell, T. Lancaster, F. Xiao, F.L. Pratt, P.J. Baker, Y. Kohama, J. Singleton, S.H. Lapidus, K.H. Stone, P.W. Stephens, K. Wierschem, T.J. Woods, C.J. Villa, K.E. Carreiro, H. E. Tran, J.L. Manson, Inorg. Chem. 55 (2016) 3515–3529.
[35] Q.-L. Wang, F. Qi, G. Yang, D.-Z. Liao, G.-M. Yang, H.-X. Ren, Z. Anorg. Allg. Chem. 636 (2010) 634–640.
[36] B.M. Huddart, J. Brambleby, T. Lancaster, P.A. Goddard, F. Xiao, S.J. Blundell, F.L. Pratt, J. Singleton, P. Macchi, R. Scatena, A.M. Barton, J.L. Manson, Phys. Chem. Chem. Phys. 21 (2019) 1014–1018.
[37] J.L. Manson, J.A. Schlueter, K.E. Garrett, P.A. Goddard, T. Lancaster, J.S. Moeller, S.J. Blundell, A.J. Steele, I. Franke, F.L. Pratt, J. Singleton, J. Bendix, S.H. Lapidus, M. Uhlarz, O. Ayala-Valenzuela, R.D. McDonald, M. Gurak, C. Baines, Chem. Commun. 52 (2016) 12653.
[38] (a) L.H.R. Dos Santos, A. Lanza, A.M. Barton, J.D. Brambleby, W.J.A. Blackmore, P.A. Goddard, F. Xiao, R.C. Williams, A. Vaidya, T. Lancaster, F.L. Pratt, S.J. Blundell, J. Singleton, J.L. Manson, P. Macchi, J. Am. Chem. Soc. 138 (2016) 2280;
(b) P.R. Hammar, M.B. Stone, D.H. Reich, C. Broholm, P.J. Gibson, M.M. Turnbull, C.P. Landee, M. Oshikawa, Phys. Rev. B 59 (1999) 1008–1015;
(c) D.B. Losee, H.W. Richardson, W.E. Hatfield, J. Chem. Phys. 59 (1973) 3600–3603.
[39] P.A. Goddard, J. Singleton, I. Franke, J.S. Moeller, T. Lancaster, A.J. Steele, C.V. Topping, S.J. Blundell, F.L. Pratt, C. Baines, J. Bendix, R.D. McDonald, J. Brambleby, M. Lees, S.H. Lapidus, P.W. Stephens, B. Twamley, M.M. Conner, K. Funk, J.F. Corbey, H.E. Tran, J.A. Schlueter, J.L. Manson, Phys. Rev. B 93 (2016) 094430.
[40] T. Lancaster, P.A. Goddard, S.J. Blundell, F.R. Foronda, S. Ghannadzadeh, J.S. Möller, P.J. Baker, F.L. Pratt, C. Baines, L. Huang, J. Wosnitza, R.D. McDonald, K. A. Modic, J. Singleton, C.V. Topping, T.A.W. Beale, F. Xiao, J.A. Schlueter, A.M. Barton, R.D. Cabrera, K.E. Carreiro, H.E. Tran, J.L. Manson, Phys. Rev. Lett. 112 (2014) 207201.
[41] J.L. Manson, J.A. Schlueter, H.I. Southerland, B. Twamley, K.A. Funk, T. Lancaster, S.J. Blundell, F.L. Pratt, P.J. Baker, J. Singleton, R. McDonald, P.A. Goddard, P. Sengupta, C.D. Batista, L. Ding, S. Cox, C. Lee, M.-H. Whangbo, C. Baines, D. Trial, J. Am. Chem. Soc. 131 (2009) 6733.
[42] C.R. Groom, I.J. Bruno, M.P. Lightfoot, S.C. Ward, Acta Crystallogr. B 72 (2016) 171–179.
[43] T. Lancaster, S.J. Blundell, P.J. Baker, M.L. Brooks, W. Hayes, F.L. Pratt, J.L. Manson, M.M. Conner, J.A. Schlueter, Phys. Rev. B 99 (2007) 267601.
[44] R.A.J. Driessen, F.B. Hulsbergen, W.J. Vermin, J. Reedijk, Inorg. Chem. 21 (1982) 3594–3597.
[45] O. Kahn, Molecular Magnetism, Wiley-VCH, Weinheim, 1993.
[46] J.L. Manson, J. Brambleby, P.M. Spurgeon, J.A. Villa, J. Liu, S. Ghannadzadeh, F. Foranda, P.A. Goddard, J. Singleton, T. Lancaster, S.W. Clark, I.O. Thomas, F. Xiao, R.C. Williams, F.L. Pratt, S.J. Blundell, C. Baines, C. Campana, B. Noll, Sci. Rep. 8 (2018) 4745.
[47] X.-F. Zhang, S. Gao, L.-H. Huo, Z.-Z. Lu, H. Zhao, Acta Crystallogr. E60 (2004) m1367–m1369.
[48] W. J. A. Blackmore, S. M. P. Curley, R. C. Williams, P. A. Goddard, J. Singleton, S. Birnbaum, A. Ozarowski, J. A. Schlueter, Y.-S. Chen, D. Y. Villa, J. L. Manson, in preparation.